


CRITICAL REVIEW

Large-scale structures of wall-bounded turbulence in single- and two-phase flows: advancing understanding of the atmospheric surface layer during sandstorms

Hongyou Liu¹  and Xiaojing Zheng^{1,*} 

¹Centre for Particle-laden Turbulence, Lanzhou University, Lanzhou 730000, PR China

*Corresponding author. E-mail: xjzheng@lzu.edu.cn

Received: 29 December 2020; **Revised:** 24 May 2021; **Accepted:** 8 June 2021

Keywords: Particle/fluid flow; Multiphase flow; Turbulent boundary layers; Atmospheric flows; Environmental fluid dynamics

Abstract

In recent years, observations of the atmospheric surface layer have greatly promoted research on high-Reynolds-number wall-bounded turbulence, especially observations of wind-blown sand flows/sandstorms, which are typical sand-laden two-phase flows; these successes have advanced the science of gas–solid two-phase wall-bounded turbulence to very-high-Reynolds-number conditions. Based on a review of existing atmospheric surface layer observations and the development process, this paper summarizes the important promoting effect played by these observations in understanding the very-large-scale structure characteristics, turbulent kinetic energy fraction and amplitude modulation effect, and in reconstructing the spatial electric field under high-Reynolds-number wall turbulence. This review focuses on the main successes achieved by the observation of sand-laden two-phase flows and the three-dimensional turbulent flow field, especially in the streamwise direction. Finally, some suggestions and outlooks for further research on particle-laden two-phase wall-bounded turbulence under high-Reynolds-number conditions are presented.

Impact Statement

The atmospheric surface layer flow represents some of the highest Reynolds number conditions that can be achieved terrestrially, and the wind-blown sand flow/sandstorm is a typical sand-laden two-phase flow in nature. Thus, the atmospheric surface layer is usually seen as a useful benchmark for high-Reynolds-number particle-free and particle-laden flow experiments. Studies based on observations of the atmospheric surface layer, especially observations of wind-blown sand flows/sandstorms, promote progress in investigating the high-Reynolds-number wall-bounded turbulence and gas–solid two-phase flows that are prevalent and important in many engineering and scientific applications. In addition, the obtained results may provide scientific basis for accurately predicting and optimally designing the prevention measures of wind-blown sand movements and sandstorms.

1. Introduction

Wind-blown sand flows/sandstorms are common, natural flows that occur on sandy surfaces and present various hazards, which include wind erosion and desertification of soil, air pollution, and even casualties

and property losses (Zheng, 2009). Wind-blown sand flows/sandstorms are mechanically characterized by a particle–gas two-phase flow experiencing wall turbulence, with a friction Reynolds number Re_τ ($Re_\tau = U_\tau \delta / \nu$, where U_τ , δ and ν denote the friction velocity, the boundary layer thickness and the kinematic viscosity of the fluid, respectively) reaching up to 10^6 and the turbulence degree can reach 19 % at a height of 0.9 m (Wang, Gu, & Zheng, 2020). Although researchers in the fields of geosciences and atmospheric sciences have been observing and researching wind-blown sand flows/sandstorms for many decades (Bagnold, 1941; Kaimal & Wyngaard, 1989; Martin & Kok, 2018), despite being necessary, comprehensive field observations of wind-blown sand flows/sandstorms are scarce because these flows are highly nonlinear and complex, with multiphase, multiscale, multiphysical coupling characteristics and a high Reynolds number. Furthermore, turbulent flows and multiphase flows constitute two of the most challenging topics in fluid mechanics, and when combined, they pose a formidable challenge, even in a dilute and dispersed regime (Balachandar & Eaton, 2010). Accordingly, numerous reviews on wall-bounded turbulence, such as those by Robinson (1991), Marusic, McKeon, et al. (2010), Smits, McKeon, and Marusic (2011), Dennis (2015) and Wallace (2016), all agree that experimental data obtained at high Reynolds numbers are needed to better understand the dynamics of turbulence, to validate previously proposed models and to predict high-Reynolds-number flows.

In recent years, high-Reynolds-number wall turbulence has gradually become an active research topic. Consequently, many challenges remain with regard to the theory, scaling laws, physical processes, experimental techniques and numerical simulations of such wall turbulence (Smits et al., 2011). The first obstacle is understanding the effect of the Reynolds number on high-Reynolds-number wall turbulence. As the Reynolds number increases, some turbulence characteristics may appear as new phenomena that are different from the basically accepted theories, scaling laws and physical mechanisms corresponding to low-Reynolds-number wall turbulence. These new phenomena include the coupling and superposition of turbulent motions at different scales, the transport and dissipation of turbulent energy, the interactions between turbulence and particles, and the transport of heat, mass, momentum and energy. For example, in the case of a high Reynolds number, the lower boundary of the logarithmic region is dependent on the Reynolds number (Klewicki, Fife, & Wei, 2009; Marusic, Monty, Hultmark, & Smits, 2013), which is different from the fixed value considered in the case of a low Reynolds number; moreover, the Kármán constant κ in the logarithmic velocity profile tends to be a constant different from that at a low Reynolds number with an increase in the Reynolds number (Nagib & Chauhan, 2008). In addition, the inner-scaled streamwise turbulence intensity has a second peak farther from the wall in high-Reynolds-number flow (Morrison, McKeon, Jiang, & Smits, 2004), which is different from the single peak observed at low Reynolds numbers, and this second peak is closely related to the very-large-scale motions (VLSMs) that are unique to high-Reynolds-number flows. The turbulent motions are termed VLSMs if their lengths are greater than $\pi\delta$, nominally (Balakumar & Adrian, 2007; Guala, Hommema, & Adrian, 2006), and the VLSMs are conjectured to result from the coherent alignment of large-scale motions (LSMs, having lengths up to $0.1 - 1\pi\delta$) in the form of turbulent bulges or packets of hairpin vortices (Kim & Adrian, 1999).

Concerning the second challenge, laboratory measurements and numerical simulations are subject to various limitations at high Reynolds numbers. Indeed, special equipment was manufactured to obtain high-Reynolds-number flows; several representative high-Reynolds-number turbulence experimental facilities are listed in Table 1. However, these facilities are not only very expensive to construct but also have high operating costs. Furthermore, although a superpipe can realize a flow of $Re_\tau \sim O(10^5)$, experimental results at this Reynolds number have yet to be reported owing to the limitation on the measurement accuracy. On the other hand, direct numerical simulation (DNS) requires a sufficiently large computational grid to capture the features at the largest scales, yet the grid must also be fine enough so that the grid size is smaller than the smallest dissipation scale within the flow. The required grid points are proportional to $Re^{37/14}$ (Choi & Moin, 2012) in DNS, drastically increasing the computational cost. To date, the highest Re_τ values currently available by DNS in a turbulent boundary layer (TBL, Sillero, Jimenez, & Moser, 2013, 2014), pipe (Ahn, Lee, Lee, Kang & Sung, 2015) or channel (Hoyas, Oberlack, Kraheberger, & Alcantara-Avila, 2018) are of the order of $O(10^3)$, which is 2–3 orders of

Table 1. Representative high-Reynolds-number equipment.

Equipment	Flow type	Highest Re_τ	Reference
Princeton University, Superpipe	Pipe	500 000	Kim and Adrian (1999)
Kungliga Tekniska Högskolan (KTH), Minimum Turbulence Level (MTL)	TBL	14 000	Österlund, Johansson, Nagib, and Hites (2000)
Illinois Institute of Technology, National Diagnostic Facility (NDF)	TBL	22 000	Nagib, Chauhan, and Monkewitz (2007)
University of Melbourne, High Reynolds Number Boundary Layer Wind Tunnel (HRNBLWT)	TBL	32 000	Nickels, Marusic, Hafez, Hutchins, and Chong (2007)
University of New Hampshire, Flow Physics Facility (FPF)	TBL	50 000	Vincenti, Klewicki, Morrill-Winter, White, and Wosnik (2013)
Center for International Cooperation in Long Pipe Experiments (CICLOPE)	Pipe	40 000	Willert, Eisfelder, Stanislas, Klinner, and Talamelli (2017)
Princeton University, High Reynolds number Test Facility (HRTF)	TBL	89 000	Vallikivi, Hultmark, and Smits (2015)

magnitude lower than the Reynolds number in most engineering applications. Additionally, for a large eddy simulation (LES, Lesieur & Métais, 1996), the reliability of both the wall model (Marusic, Mathis, & Hutchins, 2010; Piomelli & Balaras, 2002) and the sub-grid-scale (SGS) model (Meneveau & Katz, 2000) requires the support of accurate experimental high-Reynolds-number wall turbulence data.

Experiments and numerical simulations of turbulent multi-phase flows are more complex than those of single-phase flows, making them a formidable challenge. According to the particle volume fraction Φ_v (particle volume ratio in unit volume), a particle-laden flow with $\Phi_v < 10^{-3}$ is called a dilute suspension and a particle-laden flow with $\Phi_v > 10^{-3}$ is called a dense suspension, empirically (Elghobashi, 1994). The dilute suspension can be further divided into one-way coupling ($\Phi_v < 10^{-6}$), where the particles have a negligible effect on turbulence, and two-way coupling ($10^{-6} < \Phi_v < 10^{-3}$), where the momentum transfer from the particles is large enough to alter the turbulence structure. In the dense suspension, in addition to the two-way coupling between the particles and turbulence, particle/particle collision takes place because of the increased particle loading, therefore termed four-way coupling. In terms of experimental measurement, existing particle-laden turbulence experiments, such as the laser Doppler anemometer (LDA) measurements performed by Kulick, Fessler, and Eaton (1994) and Li and Neuman (2012) and particle image velocimetry (PIV) measurements performed by Khalitov and Longmire (2002), Tay, Kuhn, and Tachie (2015) and Zheng, Wang, and Zhu (2021), were mostly conducted in the laboratory. The corresponding Reynolds number Re_τ was limited to the order of $O(10^3)$. Recently, experiments performed in the wind tunnel at the St. Anthony Falls Laboratory, University of Minnesota realized a particle-suspended flow of $Re_\tau = 19\,000$ (Berk & Coletti, 2020). For fully-resolved DNS (Mola, Fawell, & Small, 2020; Pan & Banerjee, 1997), calculating the flow field around each particle drastically increases the computational cost. The previously documented maximum Reynolds number is $Re_\tau = 647$ (Ji, Munjiza, Avital, Xu & Williams, 2014). Even if the Lagrangian point-particle method is employed (Sardina et al., 2012; Vreman, 2007; Zhao, Andersson, & Gillissen, 2013), the highest Reynolds number Re_τ currently achievable is also limited to $O(10^3)$ (Richter, 2015; Wang & Richter,

2019). To improve the Reynolds number, the LES may be a feasible approach, but currently, there is no general model for describing particle-laden turbulence at high Reynolds numbers.

As the sole truly high-Reynolds-number facility, the atmospheric surface layer (ASL) is regarded as a useful benchmark for the above experiments (Guala, Metzger, & McKeon, 2011) and presents some of the highest Reynolds number conditions that can be achieved terrestrially (Marusic, McKeon, et al., 2010). The thickness of the ASL is generally 100–200 m, and even under low-wind velocity conditions, the Re_τ of an ASL flow can reach an order of magnitude of $O(10^6)$. Moreover, because it appears on a relatively large scale, the ASL can be measured without the stringent constraints on the probe resolution imposed by smaller scale boundary layers. Therefore, owing to its larger length scale, the ASL is a feasible way to observe high-Reynolds-number flows. Since the turn of the millennium, ASL observations have promoted progress in studying high-Reynolds-number wall turbulence. This progress is based mainly on the successes at the Surface Layer Turbulence & Environmental Science Test (SLTEST) site established towards the end of the last century in the western salt flats of Utah and the Qingtu Lake Observation Array (QLOA) established in 2012 in western China. The former offers mainly two-dimensional observations of clean winds without particles in the ASL in the wall-normal and spanwise directions. In contrast, the latter can perform synchronous multipoint measurements on the three-dimensional turbulent flow field (in the streamwise, spanwise and wall-normal directions) for both wind-blown sand movements and clean winds. In addition, Hong et al. (2014) and Heisel et al. (2018) successfully achieved PIV flow imaging in the ASL using natural snowfall as seeding particles.

After briefly introducing these ASL observation sites, this review will focus on the main progress based on observations of sand-laden two-phase flows and the three-dimensional turbulent flow field, especially the observations in the streamwise direction. Some topics of this review will include the dust structure in the sand-laden flow field, the effects of sand particles on the flow structure and the modulation between multiscale turbulent motions, the error and applicability of Taylor's hypothesis of frozen turbulence in estimating the length scale of VLSMs based on the measurement of streamwise arrays, and the space charge density inversion of electric fields in sandstorms. Finally, some key issues that deserve further attention are discussed.

2. Field Observations in the ASL

Meteorological and geographic observations in the ASL focus mainly on average statistics, and researchers in meteorology, oceanography and geography, which includes the physics of wind-blown sand, have observed the ASL flow on different underlying surfaces for many years. The earliest measurement of the ASL flow was performed in 1926 by British meteorologist F. J. Scrase (Scrase, 1930). A swinging plate anemometer with a frequency of approximately 1.6 Hz was used to measure the streamwise and wall-normal wind velocities at a single point. Based on the observational data, the difference in the average Reynolds stresses at different heights was analysed; the results indicated that near the wall (1.5 m), the Reynolds stress is less than one-quarter of that farther from the wall (19 m). This observation is considered classic in the history of attempting to understand how momentum is transferred in the lower atmosphere (Barad, 1964). However, the ASL wind velocity measurement in 1926 was performed only at a single point and at a low sampling rate. Unfortunately, synchronous measurements at different locations have yet to be achieved. More recently, synchronous multipoint measurements of the wind velocity, temperature and humidity in the wall-normal direction were conducted in Kansas and Minnesota in the USA (Kaimal & Wyngaard, 1989). The resulting wall-normal profiles of the velocity and temperature in the unstable stratified ASL can be used to verify and improve the Monin–Obukhov similarity theory. In general, the thermal stratifications of the ASL can be characterized by the Richardson number and the Monin–Obukhov stability parameter. However, the velocity measurement employed a wind cup at a sampling frequency of only 1 Hz, which makes it difficult to meet the high-resolution requirements for the analysis of turbulence signals. To increase the sampling rate of velocity measurements, Zeng, Cheng, Hu, and Peng (2010) employed sonic anemometers with a sampling frequency of 10 Hz to synchronously observe the wind velocity and the temperature in the wall-normal direction (at heights of



Figure 1. Observation tower employed by (Zeng *et al.*, 2010) to measure the vertical gradients in the urban boundary layer. This figure was taken from http://www.iap.ac.cn/xwzx/tpxw/201510/t20151010_4435945.html.

47, 120 and 280 m) within the urban boundary layer; a photo of the equipment is shown in [Figure 1](#). The observations revealed the local meteorology and its impact on climate, and the authors proposed turbulence parametrization schemes for global weather forecasting models. Nevertheless, although the sampling frequency was increased, the underlying surface of the urban boundary layer and the flow environment were more complicated. Hence, their results are difficult to compare with the properties of the canonical flat TBL and thus cannot be used in the study of high-Reynolds-number wall turbulence.

Geographical observations of wind-blown sand flows in the ASL began with [Bagnold \(1941\)](#), who laid the foundations of wind-blown sand physics. Bagnold conducted field measurements on the wind velocity and sediment transport rate under wind-blown sand flows with a focus on measuring the latter. Bagnold's quantitative study on the physical mechanisms responsible for the formation and evolution of sand dunes created a precedent for the study of geomorphological dynamics and has since influenced researchers in various fields of wind-blown sand physics. However, measurement of the wind velocity in the ASL is performed to obtain the average velocity profile. Therefore, Pitot tubes distributed in the wall-normal direction (2.54, 10.16, 40.64 and 162.56 cm) were employed to measure the wind velocity at a sampling frequency of approximately 0.017–0.0056 Hz (the corresponding sampling interval is approximately 1–3 min). However, such a low sampling frequency makes it difficult to study high-Reynolds-number wall turbulence. Subsequently, many researchers observed the sediment flux and its influencing factors while focusing on the sediment transport rate, wind erosion, lift-off velocity of sand particles and threshold wind velocity of sand motion; details can be found in the paper by [Zheng \(2009\)](#). In summary, both in meteorology and geography, ASL flow observations usually involve the average velocity; furthermore, the sampling frequency is relatively low and the underlying surface of the boundary layer is generally complex, which makes it difficult to analyse high-Reynolds-number wall

turbulence. In addition, single-point or wall-normal-distributed measurements were employed, which cannot meet the requirements for analysing the spatial structure of such flow.

The ASL observations used to study high-Reynolds-number wall-bounded turbulent flow are highlighted by the SLTEST site, the details of which are provided by Metzger (2002). Unlike observations in atmospheric sciences and geosciences, the observational data acquired at the SLTEST site can be used to investigate high-Reynolds-number wall-bounded turbulent flows because this site is located on the dry lake bed of the Great Salt Lake in Utah, which has a flat and open surface, and the sampling frequency of the wind velocity is relatively high (20 Hz). However, owing to the surface conditions in this area and the low wind velocity, the flow field comprises a single phase and is free of particles. The measurement array installed at the SLTEST site is shown in Figure 2, which shows that the SLTEST array can perform synchronous multipoint measurements in the spanwise and wall-normal directions, that is, measurements of the two-dimensional turbulent flow field. For example, using steady wind data obtained at the SLTEST site with $Re_\tau \sim 6 \times 10^5 - 3 \times 10^6$ for approximately 70 h under different stratification conditions (Chauhan, Hutchins, Monty, & Marusic, 2013; Metzger & Klewicki, 2001), the turbulent statistics in the ASL were confirmed to exhibit scaling laws that are generally representative of the canonical zero-pressure-gradient flat TBL (Kunkel & Marusic, 2006). This indicates that the high-quality near-neutral ASL data acquired after applying a strict data processing procedure can be valid to study the canonical TBL, although the ASL flow may be affected by weather and environmental factors; the wind velocity and direction are uncontrollable and may be affected by significant thermal instability. In addition, based on the ASL data obtained at the SLTEST site, researchers found that VLSMs exist in the ASL (Hutchins, Chauhan, Marusic, Monty, & Klewicki, 2012; Hutchins & Marusic, 2007a; Marusic & Hutchins, 2008), with an inclination angle independent of the Reynolds number but significantly dependent on the thermal stability (Chauhan et al., 2013; Marusic & Heuer, 2007). Researchers also found that the inner peak of turbulent kinetic energy increases with the Reynolds number (Metzger & Klewicki, 2001), the turbulent kinetic energy exhibits log-linear behaviour with the wall-normal distance (Marusic et al., 2013) and LSMs/VLSMs modulate the amplitude of small-scale energy in the ASL (Guala et al., 2011; Mathis, Hutchins, & Marusic, 2009). As is evident, research based on SLTEST measurements has greatly promoted the understanding of wall turbulence with a high Reynolds number. However, owing to the lack of measurements in the streamwise direction, the applicability of Taylor's hypothesis in the ASL has not been verified. Furthermore, because the SLTEST array can obtain only particle-free fluctuating velocity data, high-Reynolds-number two-phase wall-bounded turbulence has not been investigated. In addition, the short duration of the measurements at the SLTEST site and the relative scarcity of data make it difficult to obtain reliable turbulence statistics under high-Reynolds-number conditions.

Unlike the SLTEST site, the QLOA is a unique field observation station that can achieve synchronous measurements of the electric field strength and the three-dimensional (streamwise, spanwise and wall-normal directions) wind velocity, sand concentration, temperature and humidity within the three-dimensional turbulent ASL flow, as detailed by Wang and Zheng (2016). The QLOA site is flat and open, and skirts the path of strong northwest-moving monsoons and sandstorms. Therefore, the QLOA can not only observe high-Reynolds-number single-phase, particle-free flows but also conduct measurements on typical sand-laden two-phase wall-bounded turbulence, such as wind-blown sand flows/sandstorms. These sand-laden two-phase flow data make it possible to analyse the effects of particles on the statistical and structural characteristics of the flow field under high-Reynolds-number conditions and provide support for studies on the dust structure and transport in two-phase flows.

Figure 3 presents a photograph of the QLOA, which consists of a main tower with a height of 32 m, 11 and 12 auxiliary towers with a height of 5 m arranged parallel to the upwind direction of the incoming flow (that is, northwest–southeast) and the spanwise direction (which is orthogonal to the incoming flow), respectively, and another 11 auxiliary towers oriented east–west to capture another possible incoming flow direction. Compared with the SLTEST site, the QLOA incorporates two streamwise arrays arranged along different incoming flow directions. Therefore, the QLOA can not only acquire two-dimensional ASL observations in the wall-normal and spanwise directions but also realize synchronous measurements in the streamwise direction. Thus, the QLOA provides three-dimensional observations of



Figure 2. Measurement array installed at the SLTEST site. This figure was adapted from *Hutchins et al. (2012)*.

the ASL flow in a spatial domain of 390 m in the streamwise direction, 60 m in the spanwise direction and 30 m in the wall-normal direction. The observation array in the streamwise direction facilitates the measurement of the streamwise length scale of the VLSMs in the ASL and accordingly provides the error and applicability of Taylor's hypothesis in estimating the scale of the VLSMs. Moreover, these three-dimensional ASL observations are helpful for inverting the spatial structures of the flow field (see the paper by [Liu, Wang, and Zheng, 2019a](#)), in which a plausible empirical model was proposed to characterize the general shape of the three-dimensional large log-layer structure), dust concentration and electric field.

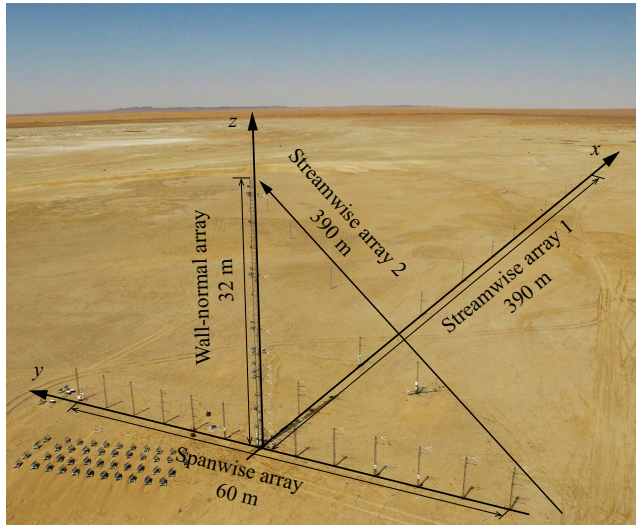


Figure 3. Photograph of the QLOA.

To achieve the high-frequency synchronous measurement of multiple physical quantities, the QLOA is equipped with various measuring equipment, such as sonic anemometers (Gill Instruments R3-50 and Campbell CSAT3B) operating at a sampling frequency of 50 Hz, aerosol monitors (TSI, DUST TRAK II-8530-EP), temperature sensors and three-dimensional vibrating-reed electric field mills (VREFMs). These VREFMs were developed by the author's research group (Zheng, 2013), and the size of the probe is only one-tenth of that of a conventional atmospheric electric field meter. Therefore, the VREFMs can be more compactly installed to measure the three-dimensional electric field in a relatively narrow region without experiencing significant mutual disturbances among the sensors. Additionally, because the measuring principle of the electric field meter is based on a vibrating capacitor, disturbances in the electric field measurements arising from sand particles impacting the electrodes of the electric field meters can be effectively reduced. The various instruments collect data through multiple data acquisition instruments, which are synchronized in time by a global positioning system (GPS), thereby realizing the synchronous measurement of multiple physical quantities, such as the three-dimensional wind velocity, temperature and electric field intensity, in the three-dimensional ASL flow field.

Taking the entire duration of the sandstorm that occurred on April 17, 2017 as an example, the multi-physical data are presented in Figure 4. These synchronous measurements are helpful for comparatively analysing the relationships among the spatial distribution characteristics of different physical quantities, thereby revealing their coupling effects, such as the relationship among the volumetric dust structure, the electric structure and the turbulence structure, and thus their interaction mechanism. To date, continuous ASL observations have been conducted at the QLOA site for 5 years since its establishment, amounting to more than 7400 h of multiphysics synchronous observational data, which include nearly 600 h of high-quality steady wind data. Of these data, approximately 120 h pertain to fluctuating velocity data in the near-neutral, particle-free ASL, while the data in the stable and unstable ASL account for approximately 302 h; in addition, there are 83 h of sand-laden fluctuating velocity data in the near-neutral ASL and 90 h of sand-laden data in the non-neutral ASL. The Reynolds numbers in sand-free and sand-laden (including sandstorms) flows may reach $Re_\tau \sim 4.7 \times 10^6$ and $Re_\tau \sim 5.4 \times 10^6$, respectively, which are the highest known Reynolds numbers in these flows.

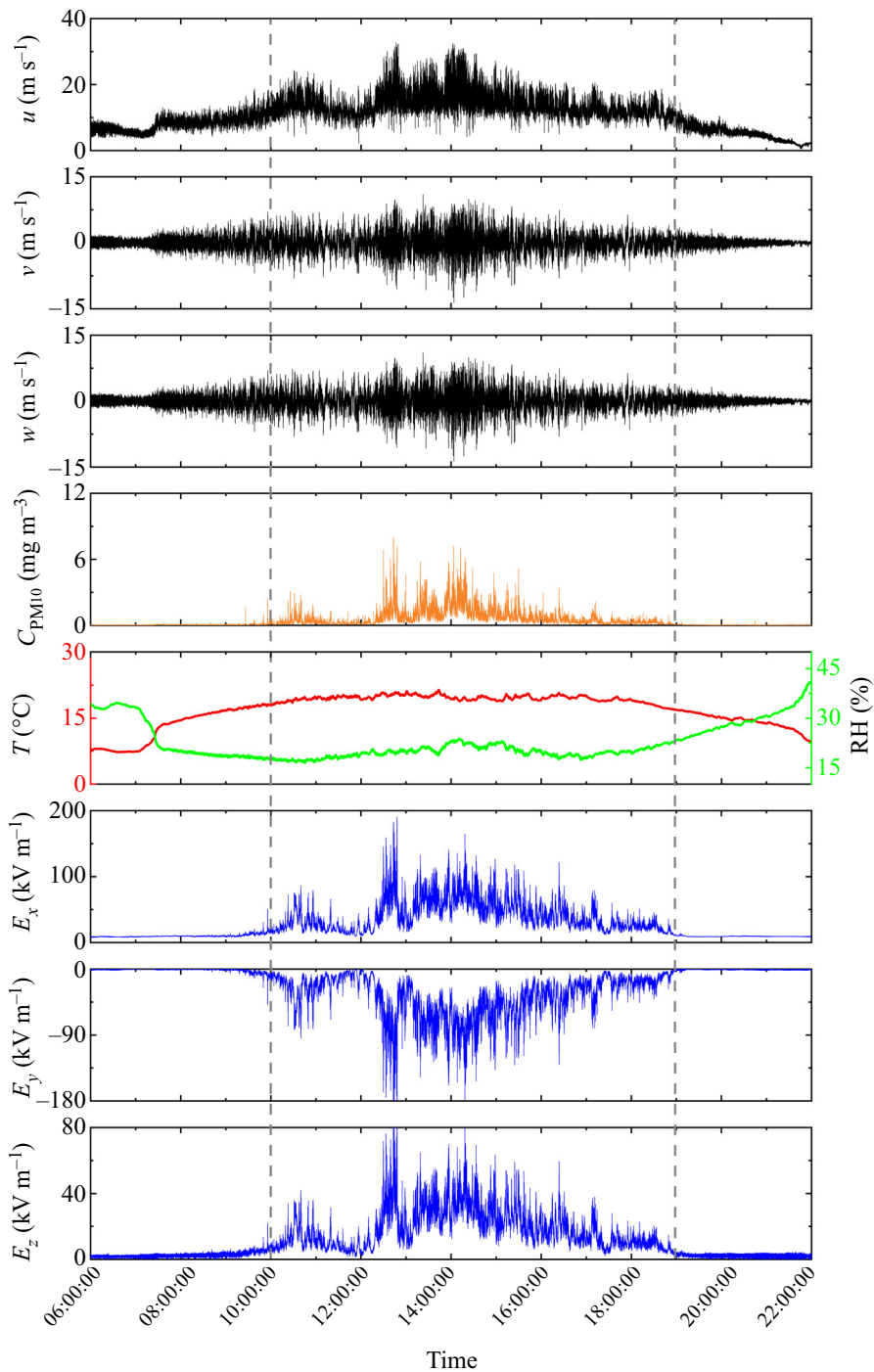


Figure 4. Continuous three-dimensional wind velocity (streamwise u , spanwise v and vertical w), PM10 concentration (C_{PM10}), temperature (T) and relative humidity (RH), and three-dimensional electric field (streamwise E_x , spanwise E_y and vertical E_z) data collected on April 17, 2017.

3. VLSMs in the Sand-Laden Two-Phase Flow

3.1. Existence of VLSMs in Sand-Laden Flows

Turbulent coherent structures represent a series of organized motions that are found in disorganized and complex turbulent flows, which mainly include hairpin vortices, quasi-streamwise vortices, inner streaks, LSMs and VLSMs, where LSMs/VLSMs are an important and perhaps dominant feature in the outer region of wall turbulence. The discovery of coherent structures in wall turbulence can be traced back to 1954, when S. Corrsin and A. L. Kistler found intermittent turbulence in the wake of a turbulent flow, which implies that turbulence is not a completely irregular and random motion (Corrsin & Kistler, 1954). These coherent structures are responsible for the generation and dissipation of turbulence, important to the understanding of turbulence dynamics (Robinson, 1991), and contribute significantly to the transport of heat, mass and momentum (Marusic, McKeon, et al., 2010). The LSMs in wall turbulence may have been found as early as the late 1950s when Grant observed long tails of time-delayed streamwise velocity fluctuations, which implied the potential presence of large-scale structures in shear turbulence (Grant, 1958). However, LSMs were not officially reported until Kovasznyai, Kibens, and Blackwelder (1970) clearly proposed the existence of LSMs on the streamwise scale reaching $2-3\delta$. Subsequently, Kim and Adrian (1999) found VLSMs on the streamwise scale exceeding 3δ or even $10-15\delta$ in wall turbulence, as shown in Figure 5. More recently, Guala et al. (2011) and Hutchins et al. (2012) detected VLSMs in the particle-free flow of the ASL based on observational data ($Re_\tau = 5 \times 10^5 - 7.7 \times 10^5$) obtained at the SLTEST site. Wang, Zheng, and Tao (2017) further found VLSMs in sand-laden flow based on observational data ($Re_\tau \sim 5 \times 10^6$) of a wind-blown sand-laden two-phase flow obtained at the QLOA. Therefore, LSMs and VLSMs (collectively known as superstructures (Hutchins & Marusic, 2007a)) are common in many different types of flows (Blackwelder & Kovasznyai, 1972; Monty et al., 2007) and are associated with the higher and lower wavenumber peaks, respectively, in the premultiplied spectrum of the streamwise velocity fluctuation (Kim & Adrian, 1999; Vallikivi, Ganapathisubramani, & Smits, 2015); therefore, these superstructures contribute significantly to the turbulent kinetic energy and Reynolds shear stress (Balakumar & Adrian, 2007; Guala et al., 2006; Wang & Zheng, 2016). Moreover, LSMs/VLSMs also play an important role in mass transport (Zheng, Zhang, Wang, Liu, & Zhu, 2013), and the complex transport pathways of dust and other pollutants in the atmosphere may be associated with the dynamics of LSMs/VLSMs (Jacob & Anderson, 2017). Therefore, the study of LSMs/VLSMs is not only of great significance to understanding wall turbulence but also helpful for revealing the physical mechanism responsible for mass transport in high-Reynolds-number wall turbulence.

As described above, VLSMs are present within the sand-laden flow field; however, similar very-large-scale structures also exist in the sand concentration scalar field in wind-blown sand flows/sandstorms. Analyses of correlation contour maps and the premultiplied energy spectra of the streamwise velocity fluctuations based on observational data obtained at the QLOA suggest the presence of VLSMs on streamwise scales exceeding 3δ in high-Reynolds-number ($Re_\tau \sim 5 \times 10^6$) sandstorm flow fields. These VLSMs exhibit very long meandering features, as shown in Figure 6a, similar to the phenomenon observed by Hutchins and Marusic (2007a) in the particle-free flow at the SLTEST site. In addition, the two-point correlation analysis of the fluctuating PM10 (particles with sizes less than $10 \mu\text{m}$) concentration measured during a sandstorm is shown in Figure 6b, which further reveals an inclined very-large-scale sand structure similar to a VLSM in the sandstorm flow field. This has been confirmed by LES results (Zhang & Zheng, 2018). The streamwise distance shown in Figure 6 is converted from the temporal lead/lag using Taylor's hypothesis, where the convection velocity of the turbulence and sand structure is taken as the local mean velocity at the corresponding wall-normal position. This is consistent with the existing method used to study the characteristic length scale of VLSMs.

3.2. Structure Inclination Angles

The LSMs/VLSMs are inclined structures that are oblique to the free stream, and the angle of inclination is usually referred to as the structure inclination angle. The structure inclination angle was originally

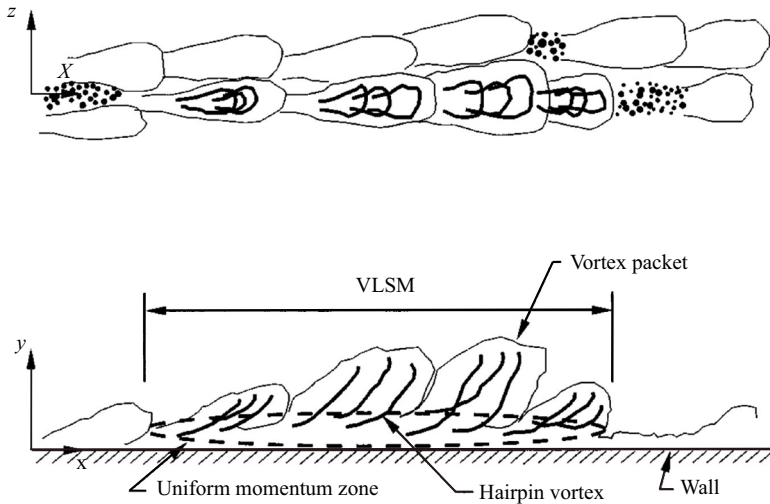


Figure 5. Conceptual model of the VLSM generation process: hairpin vortices align coherently in the streamwise direction to form hairpin vortex packets, and packets align coherently to form VLSMs. Figure adapted from *Kim and Adrian (1999)*.

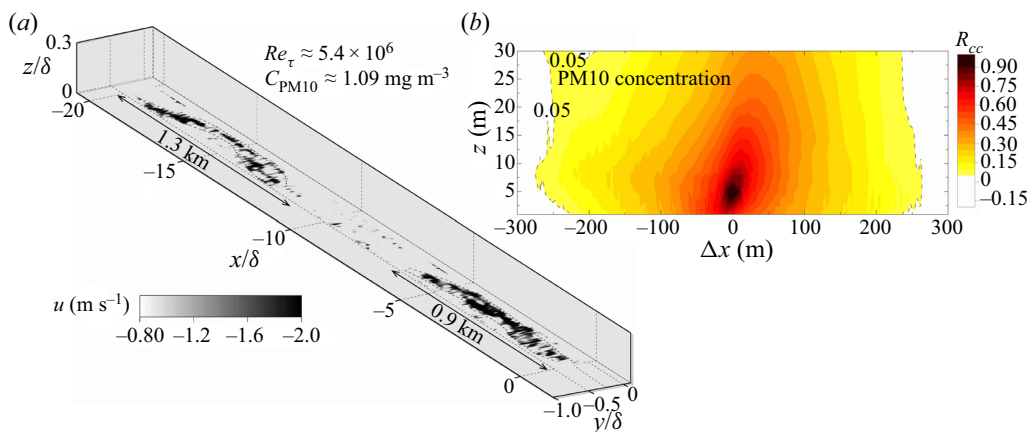


Figure 6. (a) Instantaneous streamwise velocity fluctuations across the spanwise array at $z \approx 0.033\delta$ based on observational data of a wind-blown sand-laden two-phase flow at the QLOA, with $Re_\tau \approx 5.4 \times 10^6$ and the average PM_{10} concentration $C_{PM_{10}} \approx 1.09 \text{ mg m}^{-3}$. The x -axis is reconstructed using Taylor's hypothesis and a convection velocity based on the local mean. The length marked by the arrow shows only negative u fluctuations ($u < -1 \text{ m s}^{-1}$). (b) Two-dimensional correlation maps of the fluctuating PM_{10} concentration, where the dashed line represents a correlation coefficient of 0.05.

studied by (*Kovaszny et al., 1970*), who examined the two-dimensional contour maps of two-point correlations based on the fluctuating streamwise velocity measured by hot-wire anemometers in the TBL at $Re_\tau = 1240$ and found that LSMs have a moderate tilt in the streamwise direction. The observation of LSMs inclined at a shallow angle away from the wall was subsequently confirmed by *Blackwelder and Kovaszny (1972)* and *Falco (1977)* in the TBL. LSMs/VLSMs contribute significantly to the transport of turbulence, and thus, the complex transport pathways of heat, mass and momentum may be associated with the dynamics of inclined LSMs/VLSMs (*Jacob & Anderson, 2017; Marusic, McKeon, et al., 2010*). Moreover, the structure inclination angle is vital for accurately establishing the relationship between

the velocity fluctuation and the wall shear stress (Marusic, Mathis, et al., 2010), and this relationship can be used to improve the wall model in an LES (Marusic, Kunkel, & Porte-Agel, 2001). Therefore, the inclination angle has attracted the attention of many researchers (Brown & Thomas, 1977; Chauhan et al., 2013; Kovaszny et al., 1970).

However, the structure inclination angles provided by different studies vary considerably. In the early days, Brown and Thomas (1977) inferred an 18° angle in the TBL at $Re_\tau = 3413$ from the location of the maximum correlation between the wall shear stress and the fluctuating streamwise velocities measured by a hot-film wall shear stress sensor and several hot wires. Subsequently, Head and Bandyopadhyay (1981) suggested that these large-scale structures are composed of multiple hairpin vortices inclined at 15° – 20° with respect to the wall in the TBL over the range of $500 < Re_\theta < 17500$ ($Re_\theta = U_\infty \theta / \nu$, where U_∞ and θ denote the free stream velocity and momentum thickness, respectively). Advances in techniques have provided some improvements in this topic of research; in particular, the PIV technique has provided important new information about the structure inclination angle. For example, Tomkins (1997) proposed a 12.3° angle in a laboratory TBL at $Re_\tau = 2227$, while Christensen and Adrian (2001) suggested that the inclination angle may be 13° and 14° in a channel flow at $Re_\tau = 547$ and 1734 , respectively, and Adrian, Meinhart, and Tomkins (2000) indicated that the inclination angle of a large ramp-like structure formed by hairpin vortex packets is approximately 3° – 35° , while individual hairpin vortices are inclined approximately 45° with respect to the wall.

ASL observations have played an important role in obtaining more information on the VLSM inclination angle through experiments in high-Reynolds-number flows. In the neutral marine ASL, Boppe and Neu (1995) and Boppe and Neu (1999) observed a 15° inclination angle of large-scale structures. Hommema and Adrian (2003) showed that the average inclination angle of VLSMs was 18.7° in the neutral ASL at $Re_\tau = 1.3 \times 10^6$ through a smoke visualization experiment at the SLTEST site. (Carper and Porté-Agel, 2004) also examined data from the SLTEST site and found that the structure inclination angle is approximately 16° in the neutral ASL by analysing the two-point correlations of the streamwise velocity fluctuations obtained by sonic anemometers. In addition, Morris, Stolpa, Slaboch, and Klewicki (2007) and Guala et al. (2011) suggested an 11° angle at $Re_\tau = 6 \times 10^5$ and 5×10^5 , respectively, whereas Hutchins et al. (2012) provided a 25° angle at $Re_\tau = 7.7 \times 10^5$. (Chauhan et al., 2013) indicated that the inclination angle is 13.7° in the neutral regime and varies significantly with the Monin–Obukhov stability parameter in the unstable ASL. In summary, in the neutral regime, the structure inclination angle ranges from 3° to 35° for $Re_\tau \sim O(10^3)$, while it ranges from 11° to 25° for $Re_\tau \sim O(10^6)$. Nevertheless, Marusic and Heuer (2007) postulated that the structure inclination angle does not depend on the Reynolds number given that no significant difference in the inclination angles (13.8° and 14.4° , respectively) was obtained from either a wind tunnel experiment at a low Reynolds number of $Re_\tau = 1350$ or a neutral ASL experiment at a high Reynolds number of $Re_\tau \approx 1.8 \times 10^6$. Thus, it is necessary to determine a suitable parameter to characterize the variation in the inclination angle and to ascertain the effects of particles on the inclination angle in wind-blown sand flows/sandstorms.

Studies based on long-term observations of sand-free and sand-laden flows at the QLOA have deepened the understanding of the VLSM inclination angle. A comparison between the structure inclination angles of sand-laden and sand-free flows is shown in Figure 7a, which demonstrates that the structure inclination angle in the sand-laden flow is much larger than that in the sand-free flow and decreases nearly linearly with the friction velocity (Wang et al., 2020). This linearly decreasing trend of the inclination angle is qualitatively consistent with the trend in a sand-free flow proposed by Liu, Bo, and Liang (2017). In addition, Liu, Bo, et al. (2017) provided a plausible explanation for why the friction velocity dominates the behaviour of the inclination angle: the structure inclination angle of an LSM/VLSM is actually the angle between the interface formed by two or more hairpin vortex heads (creating an LSM called a hairpin vortex packet) and the wall (Adrian et al., 2000). In the same packet, the older hairpin vortices (being larger) are more likely to encounter a faster moving fluid, and thus, the older hairpin vortices move downstream faster than the younger, smaller vortices closer to the wall (Dennis, 2015). As a consequence, the hairpin vortex packet is stretched by the velocity gradient, which

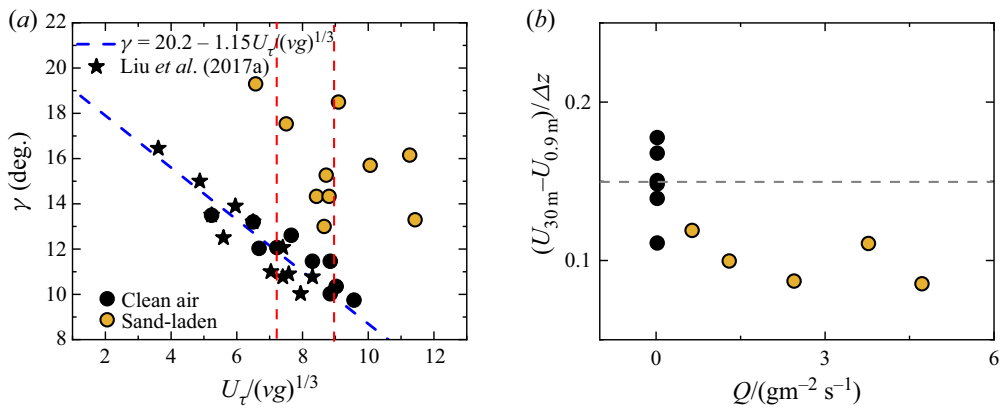


Figure 7. Variation in the structure inclination angle with the friction velocity in the neutral regime, taken from Wang et al. (2020), where the sand-free flow results are taken from Liu, Bo, et al. (2017). (b) Variation in the velocity gradient with the sand concentration in the sand-laden flow, taken from Wang et al. (2020).

forms an inclination angle. With an increase in the velocity gradient, this ‘stretching’ effect is enhanced, which results in a decrease in the inclination angle. The friction velocity reflects mainly the velocity gradient in the boundary layer. Therefore, the inclination angle decreases linearly with the friction velocity. Accordingly, the addition of a large number of sand particles into a sand-laden flow reduces the velocity gradient in the flow field, as shown in Figure 7b, which leads to an increase in the inclination angle. Note that experimental scatter is inevitably associated with these ASL measurements; however, it appears that these measurements can be used as a representation of the very-high-Reynolds-number behaviour. A detailed analysis of the effects of sand concentration on the mean shear requires more data for support. In addition to the particle concentration, the particle size has an effect on the mean shear and coherent structures. Tsuji and Morikawa (1982) found that in cases of both large particle size (with a diameter of 3.4 mm) and small particle size (0.2 mm), the particles flatten the air-velocity profile (that is, they reduce the mean shear), and the flattening of the air-velocity profile is more remarkable in the case of small particle size. With smaller particle size (0.1–0.2 mm), Righetti and Romano (2004) also observed reduced mean shear in the particle-laden turbulence. This may lead to the increased inclination angle of the large-scale coherent structure in the particle-laden turbulence, as suggested by Tay et al. (2015).

3.3. Characteristic Length Scale

The influence of the Reynolds number on the characteristic length scale of VLSMs is not clear. In the early days, Tritton (1967) examined the two-point correlation of the streamwise velocity fluctuations in the streamwise direction in a wind tunnel TBL at $Re_\tau \approx 880$ and discovered that the streamwise length scale may exceed 5δ and that the spanwise width scale is approximately 0.6δ at the top of the logarithmic region. In an LES of a channel flow ($Re_\tau \approx 640$), Moin and Kim (1982) studied the streamwise velocity correlation and inferred a streamwise length scale of approximately 6δ with a corresponding spanwise width scale of approximately 0.5δ at the wall-normal distance $z = 0.121\delta$. At the turn of the millennium, the proposal of the hairpin vortex packet model (Adrian et al., 2000; Kim & Adrian, 1999) based on experiments in a pipe (at $Re_\tau = 1058$ – 3175) and the TBL (at $Re_\tau = 355$ – 2000) contributed to better understanding the mechanism responsible for the formation of LSMs/VLSMs. The basic idea of this model is that two or more hairpin vortices are aligned coherently in the streamwise direction, which creates an LSM (called a hairpin vortex packet) with a streamwise length scale of $\sim 3\delta$; then, packets may also align with other packets to create a VLSM with a streamwise length scale of $\sim 6\delta$.

With the development of experimental facilities and measurement techniques, the observable Reynolds number of a flow has greatly increased. Notably, [Hutchins and Marusic \(2007a\)](#) compared the characteristic length scales at four different Reynolds numbers ($Re_\tau = 1120, 7610, 14380$ and 19960) by conducting experiments in the High Reynolds Number Boundary Layer Wind Tunnel (HRN-BLWT) with a spanwise array of ten hot wires and discovered that the streamwise length scale for $Re_\tau = 1120$ seems to be slightly shorter than that for the other three cases. This finding may indicate that the VLSM scale is dependent on the Reynolds number. However, the results obtained by [Hutchins et al. \(2012\)](#) from high-Reynolds-number ($Re_\tau \approx 7.7 \times 10^5$) ASL observations at the SLTEST site indicate that the outer-scaled streamwise velocity correlation agrees well with the documented laboratory TBL results provided by [Hutchins and Marusic \(2007a\)](#), which provides possible evidence that these large-scale structures scale on the boundary layer thickness up to $Re_\tau \sim O(10^6)$. Nevertheless, high-Reynolds-number experimental data are quite sparse and more work is needed.

Coherent structures exist throughout the boundary layer, and thus, it is very important to characterize the variation in the characteristic length scale with the wall-normal distance. [Tritton \(1967\)](#) and [Moin and Kim \(1982\)](#) found that the spanwise scale of the coherent structures increases with the wall-normal distance throughout the boundary layer, whereas the streamwise scale decreases with the wall-normal distance in the wake region in the TBL and channel flow at $Re_\tau = 880$ and 640 , respectively. Subsequently, [Krogstad and Antonia \(1994\)](#) published laboratory TBL results at $Re_\tau = 1850$ showing that the streamwise scale increases with the wall-normal distance according to the hyperbolic tangent function, i.e. $L_x \sim \tanh(12z/\delta)$. However, the variations in the characteristic length scale with the wall-normal distance given by different studies diverge. For example, [Tomkins and Adrian \(2003\)](#) suggested that both the streamwise and spanwise length scales linearly increase with the wall-normal distance in the logarithmic region of the TBL at $Re_\tau = 2216$. This is consistent with [Townsend's \(1976\)](#) attached eddy hypothesis because the linear growth of the eddy size with distance from the wall is a necessary condition for self-similarity, where self-similarity is an assumption of the hierarchy of attached eddies [Perry and Chong \(1982\)](#); and recently summarized by [Marusic and Monty \(2019\)](#). The conclusions obtained from studies on the TBL at $Re_\tau = 690$ – 2800 indicate that the spanwise scale of the coherent structures increases linearly throughout the TBL and that the increase is more pronounced in the logarithmic region ([Ganapathisubramani, Hutchins, Hambleton, Longmire, & Marusic, 2005](#); [Hutchins, Hambleton, & Marusic, 2005](#)). Based on experimental data in pipe ($Re_\tau = 933$ – 4355) and channel ($Re_\tau = 3178$) flows in conjunction with previously reported boundary layer data, [Monty et al. \(2007\)](#) found that the spanwise scale of the coherent structures linearly increases piecewise with the wall-normal distance (even in the wake region) for all available data, with $Re_\tau \sim O(10^3 - 10^4)$ in different types of flows, as shown in [Figure 8a](#). Recently, the DNS of a TBL at $Re_\tau \approx 920$ performed by [Lee and Sung \(2011\)](#) showed that the streamwise length scale increases as far as the top of the logarithmic region ($z/\delta = 0.2$) and then sharply decreases in the wake region, as shown in [Figure 8b](#). This behaviour may be explained by the detached eddies in the attached eddy theory. Outside the log region of a boundary layer, coherent structures (e.g. hairpin packets proposed by [Kim & Adrian \(1999\)](#)) that exist in the log region do not retain their coherence. The breakdown of these structures produces a population of smaller eddies, which may be detached eddies, vortex rings or some other outer-layer structure ([Katul & Vidakovic, 1996](#); [Perry & Marusic, 1995](#)). The length scale extracted from the two-point correlation represents the average scale of all turbulent coherent structures at a given distance from the wall. Therefore, the popular smaller scales may reduce the streamwise length scale.

Studies on flows at high Reynolds numbers and broad Reynolds number ranges based on observations of wind-blown sand flows/sandstorms at the QLOA have improved the understanding of the scale of coherent structures. The streamwise length scales calculated using the experimental data of [Wang et al. \(2020\)](#) in a wind-blown sand flow at the QLOA are shown as the yellow symbols in [Figure 9](#). The results in this figure are in good agreement with those of a sand-free flow in the ASL ([Liu, Wang, & Zheng, 2017](#)); that is, the streamwise length scale remains approximately invariant with the Reynolds number. However, combined with wind tunnel experimental data at low and moderate Reynolds numbers, [Zheng \(2020\)](#) revealed that the streamwise length scale of the coherent structures tends to become gradually

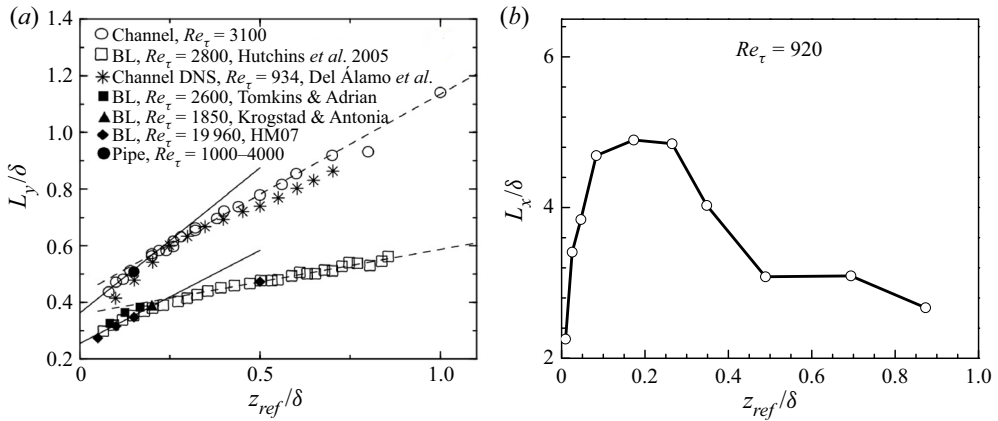


Figure 8. (a) Variation in the spanwise width scale with the wall-normal distance. Figure adapted from Monty *et al.* (2007), where the solid curves are fitted to the open symbols for $z < 0.15\delta$ and the dashed curves are fitted to the open symbols for $z > 0.4\delta$. (b) Variation in the streamwise length scale with the wall-normal distance. This figure was adapted from Lee and Sung (2011).

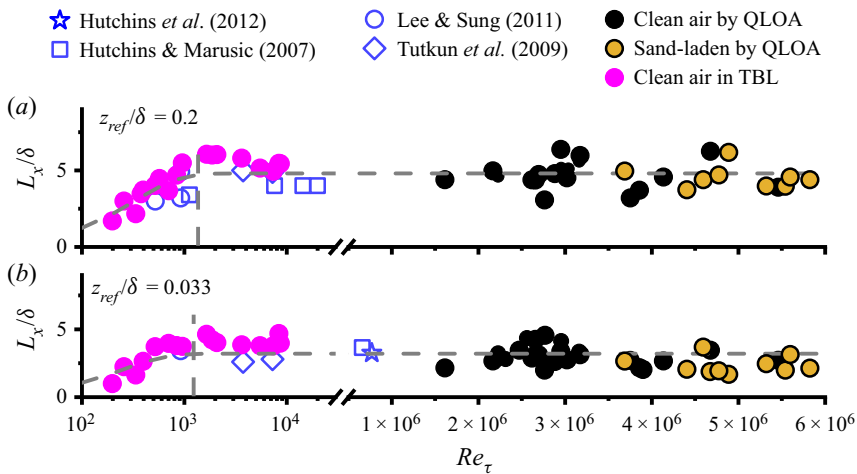


Figure 9. Variation in the streamwise length scale of the coherent structure with the Reynolds number, where the results of sand-free flows in the ASL were taken from Liu, Wang, *et al.* (2017), the wind tunnel TBL results were taken from Zheng (2020) and the sand-laden flow results were taken from Wang *et al.* (2020).

invariant with increasing Reynolds number spanning over four orders of magnitude $Re_\tau \sim O(10^2-10^6)$, as shown by the pink symbols in Figure 9. The quantitative results show that when $Re_\tau < 1200$, the streamwise length scale increases with the Reynolds number, whereas when $Re_\tau > 1200$, the outer-scaled length scale no longer varies with the Reynolds number. In addition, Wang *et al.* (2020) revealed that the streamwise length scale and wall-normal length scale of the coherent structures in sand-laden flows increase with the wall-normal distance, which is qualitatively consistent with the relatively universal law governing the evolution of the spatial length scale revealed by Liu, Wang, *et al.* (2017) using data from the QLOA of high-Reynolds-number sand-free flows. Moreover, a quantitative comparison indicates that the addition of particles to a wind-blown sand flow reduces the wall-normal length scale by approximately 40 %.

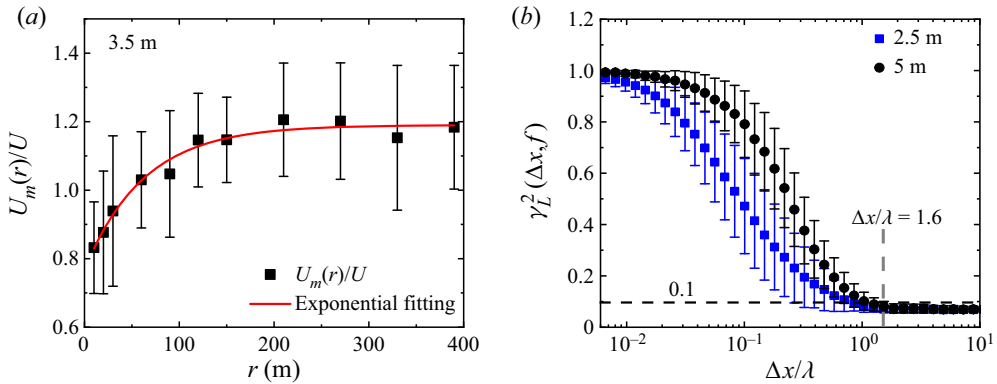


Figure 10. (a) Variation in the convection velocity with the migration distance based on QLOA data and (b) coherent spectrum analysis. The measured convection velocity and the local mean velocity are represented by U_m and U , respectively. Here, Δx is the streamwise distance, f is the frequency, and $\lambda = U_m/f$ is the streamwise wavelength.

However, the streamwise length scale of coherent structures in the ASL obtained by spatiotemporally converting the measured data through Taylor’s hypothesis is underestimated. Except for some of the flow images obtained by PIV in the laboratory (Hutchins & Marusic, 2007a; Wang, Huang, Zhang, Wang & Zhao, 2018), estimates of the streamwise length scale are still based mostly on Taylor’s hypothesis. However, Taylor’s hypothesis is applicable only on the premise that the convection velocity of the turbulence structure is consistent with the local mean velocity at the corresponding wall-normal position and that the structure does not deform during convection. Unfortunately, these assumptions are difficult to fully satisfy in actual flows, especially boundary layer flows. Therefore, the applicability of Taylor’s hypothesis has become a hotspot in turbulence research (Squire et al., 2017; see He, Jin, & Yang, 2017 for a review of relevant studies). Using the observational data from the streamwise array unique to the QLOA, Han, Wang, and Zheng (2019) reported that the directly measured streamwise length scale of the coherent structures is generally larger than that obtained by Taylor’s hypothesis (see Table 4 in Han, Wang, et al. (2019), where the maximum relative error reaches 25%). This is because the convection velocity of coherent structures in the logarithmic region of the ASL varies with the migration distance, as shown in Figure 10a, in which the convection velocity may reach 40% higher than the local mean velocity when the migration distance exceeds approximately 300 m (where the migration distance represents the spatial displacement of coherent structure along the streamwise direction). Moreover, a coherent structure in the ASL experiences complete deformation after migrating a distance 1.6 times its own scale in the streamwise direction, as shown in Figure 10b, where

$$\gamma_L^2(\Delta x, f) = \frac{|\langle U_A(x, f) \overline{U_B(x + \Delta x, f)} \rangle|^2}{\langle |U_A(x, f)|^2 \rangle \langle |U_B(x + \Delta x, f)|^2 \rangle} \tag{1}$$

is the linear coherence spectrum (Baars, Hutchins, & Marusic, 2016) of the streamwise velocity fluctuations $u_A(x, t + \Delta t/U_m)$ and $u_B(x + \Delta x, t)$, $U_A(x, f)$ and $U_B(x + \Delta x, f)$ are the Fourier transforms of $u_A(x, t + \Delta t/U_m)$ and $u_B(x + \Delta x, t)$, $\langle \rangle$ denotes ensemble averaging, the overbar indicates the complex conjugate and $||$ designates the modulus.

3.4. Turbulent Kinetic Energy of VLSMs

The contributions of VLSMs to the turbulent kinetic energy, Reynolds shear stress and transport of material are significantly greater than those of other coherent structures. Turbulence exhibits multiscale motions and the energies of different-scale motions differ. Nevertheless, the dominant position of the

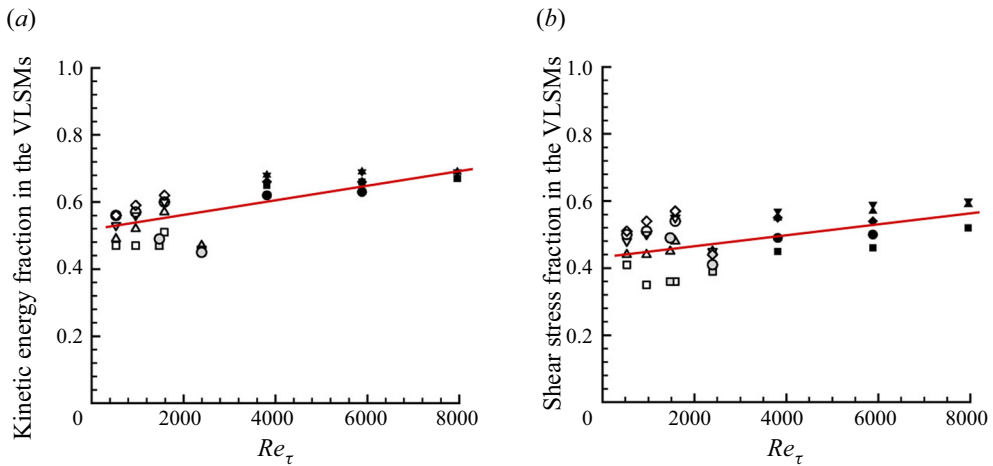


Figure 11. Variations in the fractions of (a) kinetic energy and (b) shear stress carried by VLSMs as a function of the Reynolds number for channel (open symbols), zero-pressure-gradient boundary layer (ZPGBL, grey filled symbols) and pipe (black filled symbols) flows for the following fractions: open squares, $z/\delta \sim 0.1$; open upright triangles, $z/\delta \sim 0.2$; open inverted triangles, $z/\delta \sim 0.3$; open diamonds, $z/\delta \sim 0.5$; and open circles, $z/\delta \sim 0.7$ (taken from Balakumar & Adrian (2007)).

corresponding motion in turbulence is reflected by the energy level. The LSMs/VLSMs initially received attention as a result of their large scale until Kim and Adrian (1999) analysed the energy spectra in pipes over $1058 \leq Re_\tau \leq 3175$ and noticed that the high-wavenumber and low-wavenumber peaks in the energy spectra corresponded to LSMs and VLSMs in the outer layer, respectively. Moreover, the low-wavenumber peak becomes more obvious in higher-Reynolds-number flows (Vallikivi, Hultmark, et al., 2015; Wang & Zheng, 2016), which means that the VLSMs in the outer layer have the most significant contribution to the turbulent kinetic energy in high-Reynolds-number wall turbulence, thereby becoming the dominant structural feature. Subsequently, researchers have successively investigated the energy fraction contributed by VLSMs to the total turbulent kinetic energy. For example, Morrison et al. (2004) analysed pipe flows over $1500 \leq Re_\tau \leq 1.01 \times 10^5$ and revealed that the fraction of turbulent kinetic energy caused by VLSMs can reach 50%. The pipe flow ($3815 \leq Re_\tau \leq 7959$) examined by Guala et al. (2006) indicated that the energy fraction of VLSMs can reach up to 65%, with a 50%–60% contribution to the Reynolds shear stress. Balakumar and Adrian (2007) analysed experimental data in the TBL ($1476 \leq Re_\tau \leq 2395$) and channel flow ($531 \leq Re_\tau \leq 1584$), and proposed that the contributions of VLSMs to the turbulent kinetic energy and Reynolds shear stress were approximately 40%–65% and 30%–50%, respectively; they also stated that the variations in the energy contribution and shear stress carried by the VLSMs are functions of the Reynolds number for different flows, as shown in Figure 11. Numerical simulation results in recent years support this finding. For example, a DNS ($459 \leq Re_\tau \leq 732$) in the TBL (Lee & Sung, 2011) demonstrated that the Reynolds shear stress contributed by VLSMs exceeds 45%. Furthermore, the LES results of the TBL at $Re_\tau \sim 4000$ (Deck, Renard, Laraufie, & Weiss, 2014) show that VLSMs/LSMs significantly affect the wall shear stress and contribute more than 60% of the turbulent friction coefficient (i.e. the contribution of turbulence to mean friction is obtained by the weighted integration of the Reynolds shear stress). The effect of VLSMs contributing such a high fraction of turbulent kinetic energy on the transport of material is also obviously critical. Especially in the ASL, VLSMs play a major role in the downward transport of momentum (Horiguchi, Hayashi, Adachi, & Onogi, 2012), which will significantly affect the movement of both water vapour and CO₂ (Cooper et al., 2006; Serafimovich, Thomas, & Foken, 2011).

A new mechanism that explains how the VLSM energy changes with height based on the observation results of sand-laden two-phase flows in the ASL has been proposed. The variation in the energy fraction

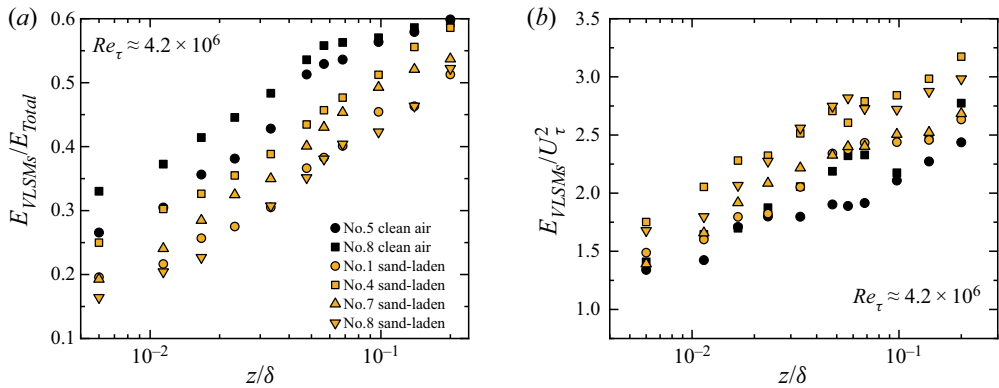


Figure 12. Variations in the contributions of VLSMs to the turbulent kinetic energy in a high-Reynolds-number flow in the ASL with height: (a) the energy fraction contributed by VLSMs to the total turbulent kinetic energy and (b) the normalized energy contributed by VLSMs in clean air (black) and sand-laden (yellow) flows, taken from Wang et al. (2020).

of VLSMs with height is very important because VLSMs commonly exist in the entire outer layer. However, this topic has been the subject of relatively little research. Recently, Wang et al. (2020) analysed the influences of sand particles on the turbulent kinetic energy and energy fraction of VLSMs based on the observational data of sand-laden two-phase flows from the QLOA, as shown in Figure 12 (yellow dots). The turbulent kinetic energy and energy fraction of VLSMs in high-Reynolds-number sand-laden flows increase with an approximately log-linear behaviour with height, which is qualitatively consistent with the particle-free flow results. However, a quantitative comparison shows that the normalized turbulent energy of VLSMs increases while the energy fraction of VLSMs decreases in sand-laden flows, which means that sand particles not only increase the energy of VLSMs but also significantly increase the total streamwise turbulent kinetic energy in sand-laden flows. The corresponding particle-free flow results can be found in the paper by Wang and Zheng (2016), who revealed the mechanism by which the energy of VLSMs and the energy fraction increase with the wall-normal distance in an approximately log-linear manner, as shown in Figure 12 (black dots). The energy fraction of VLSMs can reach 60% at the top of the logarithmic layer ($z = 0.2\delta$), which is larger than the energy fractions (approximately 40%–50% over $Re_\tau \sim O(10^2) - O(10^3)$) obtained during the experiment conducted in the TBL by Balakumar and Adrian (2007) and Lee and Sung (2011), which also means that the contribution of VLSMs to the turbulent kinetic energy becomes more obvious at higher Reynolds numbers.

Another important impact of research on the energy fraction contributed by VLSMs to the process of wind-blown sand flows/sandstorms is to reveal the nature of the meteorological phenomenon known as ‘gusty wind’. In 1983, the World Meteorological Organization (WMO) defined gusty wind as a fluctuation that occurs approximately once every several minutes (WMO, 1983). Moreover, Zeng et al. (2010) defined gusty wind as having a fluctuation period of 1–10 min under neutral stratified conditions. According to the analysis of observational data regarding the urban boundary layer, it has been proposed that gusty wind is coherent and plays an important role in the transport of both sand and dust. Based on sand-laden flow data from the QLOA, Gu, Wang, Zhu, and Zheng (2019) compared the scales of VLSMs and LSMs with those of gusty wind in normalized energy spectra. They found that meteorological gusty wind contains a large number of synoptic waves but is missing the VLSMs and LSMs that have considerable contributions to the turbulent kinetic energy. In fact, most VLSMs and all LSMs are forfeited by gusty wind, especially under high-wind velocity condition, and the lost contributions of VLSMs and LSMs can reach 50%.

4. Amplitude Modulation and Its Application

In addition to the ubiquity and importance of LSMs/VLSMs, researchers pay attention to these outer-region structures because they have a significant amplitude modulation effect on small-scale near-wall motions (Brown & Thomas, 1977; Rajagopalan & Antonia, 1980). The discovery that LSMs/VLSMs modulate the amplitudes of small-scale motions not only contributed to a better understanding of the mechanism responsible for the production of near-wall turbulence (i.e. this process is not completely ‘autonomous’ when referring to the near-wall cycle (Jiménez & Pinelli 1999; Schoppa & Hussain, 2002)) but also provided an effective way to predict the behaviour of near-wall turbulent motions (Marusic & Hutchins, 2011; Marusic, Mathis, et al., 2010; Marusic et al., 2013). That makes sense because the scales of the two kinds of structures are different enough for the near-wall elementary structures to spend most of their ‘lives’ in an environment defined by a single large-scale modulation (Jiménez, 2013). In addition, the modulation effect of LSMs/VLSMs leads to a weakened control effectiveness on near-wall coherent structures (Deng, Huang, & Xu, 2016), and thus, manipulating the LSMs/VLSMs may provide an effective approach for controlling the turbulence (Hwang & Sung, 2017). Therefore, amplitude modulation has recently become a research hotspot and has attracted the attention of many researchers (Jacobi & McKeon, 2013; Luhar, Sharma, & McKeon, 2014; Talluru, Baidya, Hutchins, & Marusic, 2014). In summary, studies on amplitude modulation may be divided into three stages: the early discovery of this phenomenon, quantitative research, and recent applications and promotion.

The phenomenon of amplitude modulation is common in different types of flows. Initially, Brown and Thomas (1977) compared low-frequency fluctuations with rectified high-frequency smoothed signals in the TBL at $Re_\tau = 3413$ and found a high-frequency large-amplitude fluctuation occurring near the maximum in the slowly varying part of the signal, which indicates that the low-frequency fluctuation amplitude is associated with high-frequency fluctuation. In numerous different types of shear flows (including boundary layers, mixing layers, wakes and jets), Bandyopadhyay and Hussain (1984) also found significant coupling between scales in all flows by decomposing the streamwise velocity fluctuation and examining the correlations between the low-frequency and the high-frequency components. Recently, amplitude modulation was highlighted by Hutchins and Marusic (2007b), who provided a detailed description of the amplitude modulation process; that is, the amplitudes at small scales were larger within large-scale positive fluctuations, whereas the amplitudes at small scales became relatively quiescent within large-scale negative fluctuations.

The amplitude modulation coefficient, as a mathematical tool, was originally proposed by Mathis et al. (2009). The amplitude modulation coefficient can quantify the degree of the amplitude modulation effect of LSMs/VLSMs on small-scale motions. The corresponding flow chart of the complete decoupling procedure is illustrated in Figure 13. Mathis et al. (2009) compared the results of one- and two-point analyses and suggested that the single-point amplitude modulation coefficient provides a reasonable estimate of the degree of modulation. Based on this quantitative method, Mathis et al. (2009) and Mathis, Monty, Hutchins, and Marusic (2009) examined HRNBLWT ($Re_\tau = 2800\text{--}19\,000$), pipe ($Re_\tau = 3015$), channel ($Re_\tau = 3005$) and ASL ($Re_\tau = 6.5 \times 10^5$) experimental data and found that the amplitude modulation coefficient exhibits almost no difference between internal and external wall-bounded flows but exhibits strong dependence on the Reynolds number and wall-normal distance. Furthermore, the amplitude modulation coefficient increased in a log-linear fashion with the Reynolds number in the buffer layer ($20 < z^+ < 100$), but a more significant influencing factor (i.e. the wall-normal distance) has not yet been considered.

The application of amplitude modulation in the prediction model of near-wall turbulent motion further highlights the importance of the amplitude modulation effect. Based on studies of the amplitude modulation coefficient, Marusic, Mathis, et al. (2010) and Mathis, Hutchins, and Marusic (2011) proposed a time series predictive model for the near-wall fluctuating streamwise velocity; the equation is shown in Figure 14. Subsequently, Marusic and Hutchins (2011), Inoue, Mathis, Marusic, and Pullin (2012) and Mathis, Marusic, Chernyshenko, and Hutchins (2013) presented a fluctuating wall-shear

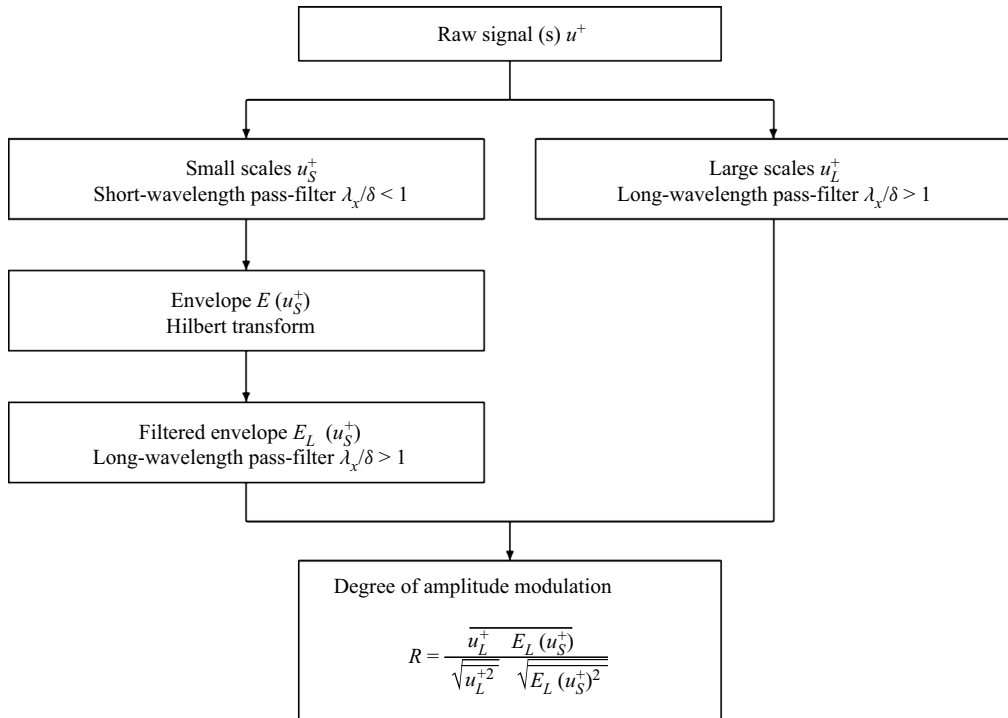


Figure 13. Flow chart for the calculation of the amplitude modulation coefficient, taken from (Mathis et al., 2009).

stress predictive model. With these predictive models, the near-wall streamwise velocity and the wall-shear stress fluctuations can be predicted using only the large-scale velocity information measured in the logarithmic region. Recently, (Howland and Yang, 2018) made theoretical predictions on the model parameters within the wall-shear stress model and then applied them to wall-modelled LES by relating the amplitude modulation process to the Townsend attached eddy hypothesis. These models are important given that it is difficult to accurately measure and simulate turbulent motion close to a solid boundary. The proposal of these near-wall models further highlights the importance of amplitude modulation; therefore, recent research on amplitude modulation still attracts the attention of many researchers.

Talluru et al. (2014) calculated the amplitude modulation coefficient of large-scale streamwise velocity fluctuations on all three components of the small-scale velocity with measurements from cross-wire probes in the TBL at $Re_\tau = 15\,000$ and found that the modulation of the small-scale energy by large-scale structures is relatively uniform across all three velocity components. Luhar et al. (2014) and Tsuji, Marusic, and Johansson (2016) investigated the amplitude modulation of pressure fluctuations and found a relatively small modulation effect between large- and small-scale pressure fluctuations. Squire, Baars, Hutchins, and Marusic (2016) and Pathikonda and Christensen (2017) explored the inner–outer interactions in rough-wall TBL flows and suggested that a rough wall increases the amplitude modulation coefficient Nadeem, Lee, Lee, and Sung (2015) and Anderson (2016) performed numerical simulations with similar results). Recently, Yao, Huang, and Xu (2018) investigated the amplitude modulation effect by the DNS of turbulent channel flows and indicated that extraordinarily high fluctuation events are provoked by the modulation effect. Salesky and Anderson (2018) presented evidence of amplitude modulation phenomena in the unstably stratified (i.e. convective) ASL by conducting an LES; they suggested that the modulation effect of the large-scale streamwise velocity decreases monotonically, while the modulating influence of the large-scale vertical velocity remains significant because the spatial attributes of the flow structures change from streamwise to vertically dominated. Wang, Pan,

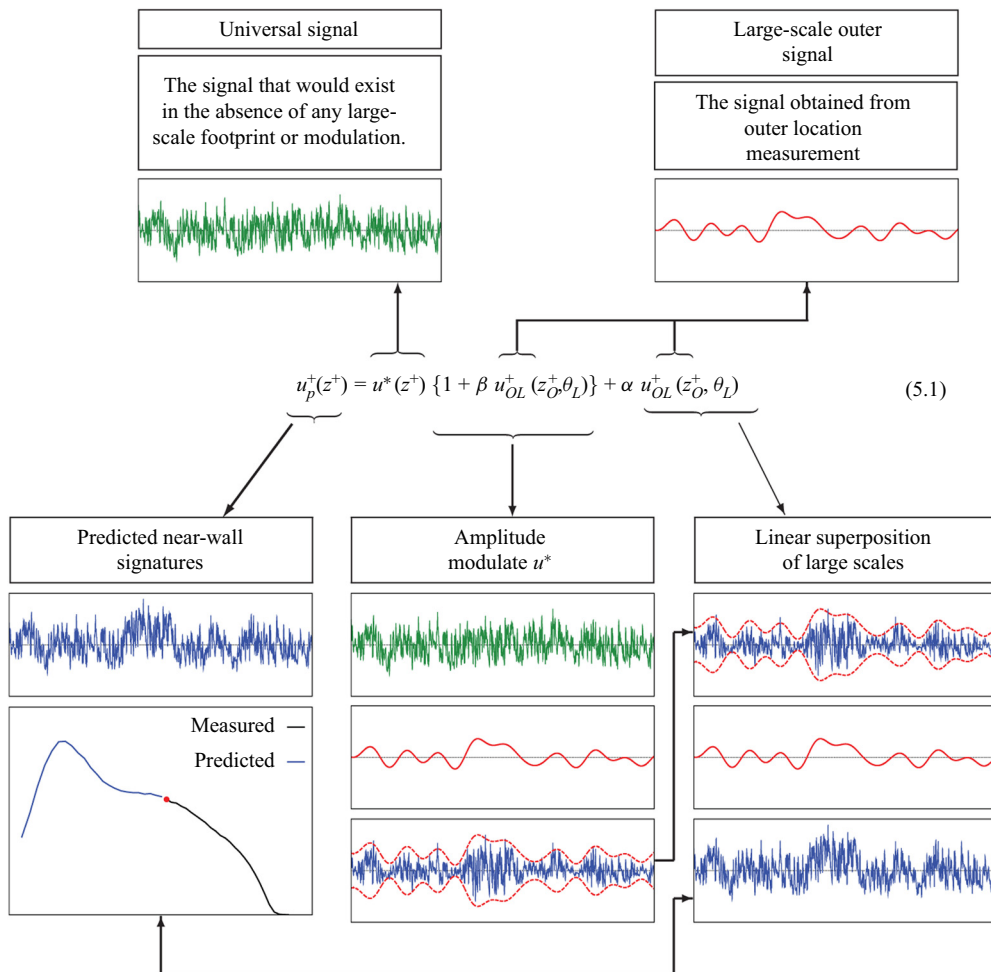


Figure 14. Mathematical formulation of the predictive model for the near-wall fluctuating streamwise velocity, taken from *Mathis et al. (2011)*.

and Wang (2020) examined the characteristics of the streamwise component of the fluctuating wall-shear stress in a smooth-wall TBL and inferred that the LSMs/VLSMs in the outer region mainly apply an amplitude modulation effect instead of a footprint effect on the wall-shear stress. However, none of the abovementioned studies on amplitude modulation involved particle-laden two-phase flows, and the decoupling procedure employed a nominal cut-off wavelength (usually taken as δ) to divide the fluctuating velocity into large- and small-scale components. Consequently, very little is known about the impacts of particles on the amplitude modulation effect and which scales of motion dominate the amplitude modulation.

Regarding the modulation effect of VLSMs, the author's team performed a detailed analysis of the sand-free and sand-laden flows of the ASL and obtained some novel results. Using experimental data with different sand concentrations in the near-neutral ASL obtained from long-term observations at the QLOA, Liu and Zheng (2020) found that VLSMs also exhibit an amplitude modulation effect on the small-scale motions in sand-laden flows, but the amplitude modulation coefficient in a sand-laden flow is significantly reduced compared with that in a sand-free flow, as shown in Figure 15. This may be because the addition of sand particles into a two-phase flow does not change the scales of the most energetic motions but does change the distribution of energy between turbulent motions at different scales. In

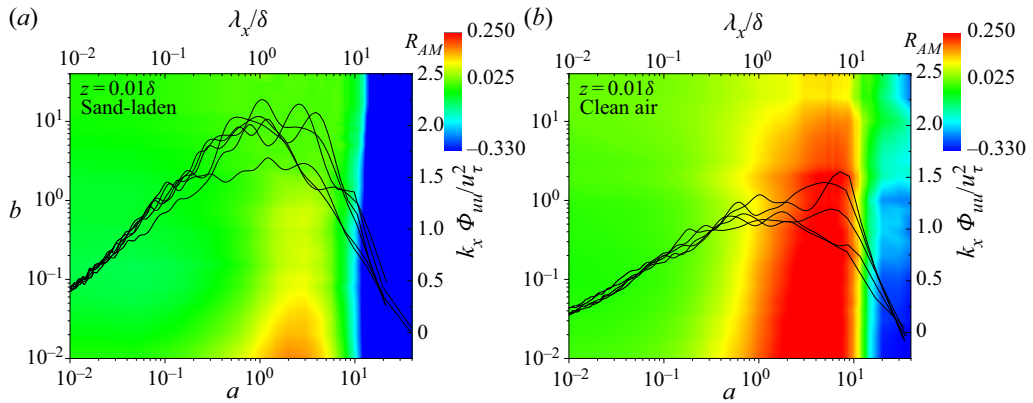


Figure 15. Colour contour maps showing the variations in the amplitude modulation coefficient with the length scales of the large-scale ($\lambda_x > a\delta$) and small-scale ($\lambda_x < b\delta$) components compared with the premultiplied energy spectra of the streamwise velocity fluctuations in a (a) sand-laden flow and (b) sand-free flow, taken from Liu et al. (2019b).

addition, Liu, Wang, and Zheng (2019b) proposed that not all of the length scales of turbulent motions have an amplitude modulation effect among them; rather, several specific motions have an effect: the most energetic motions with scales larger than the wavelength of the energy spectral peak in the lower-wavenumber region contribute significantly to the amplitude modulation effect, while the motions with small scales (shorter than the wavelength of the higher-wavenumber peak) are strongly modulated.

Marusic, Mathis, et al. (2010) proposed the Marusic–Mathis–Hutchins (MMH) near-wall wind velocity prediction model, the basic idea of which is to superpose and modulate a large-scale structure in the outer region onto a small-scale structure near the wall to predict the fluctuating wind velocity signal near the wall, which is typically difficult to measure. Therefore, this method can predict the streamwise velocity time series only below the input signal height (usually taking the centre height of the logarithmic region $z^+ = 3.9Re_\tau^{1/2}$), which is in the outer region. In the wind tunnel and ASL with boundary layer thicknesses of 0.3 and 150 m, respectively, these heights correspond to 0.02 and 0.3 m, respectively. However, in practical applications, it is often necessary to know the wind velocity fluctuation and the sand/dust transport at 2 m or even tens of metres above the input signal height. Moreover, the determination of both the MMH model parameters and the universal signal depends on high-precision calibration experiments, and the calibration process requires synchronous measurements at the measuring point in the centre of the logarithmic region and at different heights below. A hot-wire probe with high spatial and temporal resolutions is used for the wind speed measurement to ensure that the minimum viscous-scale vortices can be resolved and are close to the wall surface to ensure that the near-wall measurement signals can be obtained. However, owing to the complexity of the ASL surface and the limitations of experimental means, it is very difficult to carry out high-precision calibration experiments in the field. In addition, owing to the constant adjustment of modulation-related parameters in the process of determining the universal signal, the modulation coefficient of the large-scale fluctuation in the outer region to the near-wall standard signal is zero, so this process cannot be solved directly and the iterative adjustment process is tedious.

To describe the fluctuation characteristics of the ASL velocity field, Han, Liu, Bo, and Zheng (2019) extended the MMH model to the ASL clear-air field to obtain a modified prediction model based on the measured time series of the streamwise velocity field at a certain height z_0 (called the reference height); the purpose of this model was to predict the fluctuating streamwise velocity at any height. The modified model considers the effect of the high-Reynolds-number ASL on LSMs/VLSMs and its further effect

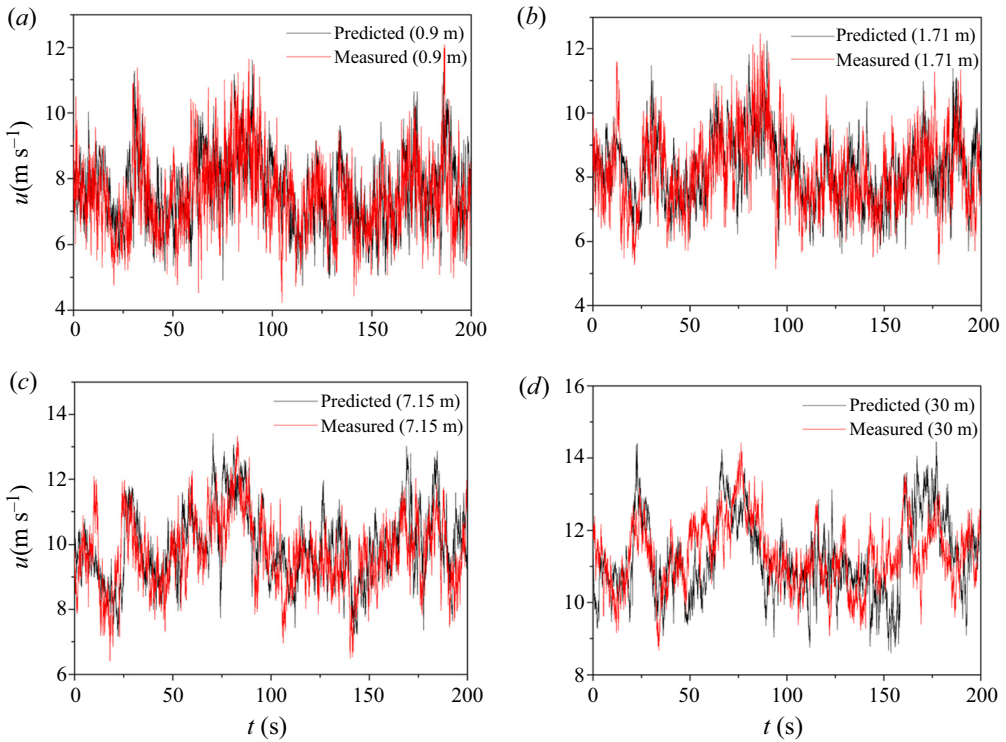


Figure 16. Comparison between the model prediction results and measured results at (a) 0.9 m; (b) 1.71 m; (c) 7.15 m; and (d) 30 m, taken from Han, Liu, et al. (2019).

on small-scale fluctuations. The model provided in Han, Liu, et al. (2019) is written as

$$u^+(z) = \bar{u}^+(z) + u_{s*}^+(z)(1 + R(z)k(z)u_{ML}^+(z_M, \gamma_L)) + k(z)u_{ML}^+(z_M, \gamma_L), \quad (2)$$

where $u^+(z)$ is the predicted streamwise velocity, $\bar{u}^+(z)$ is the mean velocity given by the logarithmic law, $u_{s*}^+(z)$ is the small-scale turbulent signal generated by the harmony superposition method, $R(z)$ is the amplitude modulation coefficient, $k(z)$ is related to the energy ratio between the large- and small-scale turbulent signals, $u_{ML}^+(z_M, \gamma_L)$ is the large-scale turbulent signal shifted forward in the streamwise direction according to the large-scale structure inclination angle γ_L , and z_M represents the centre of the logarithmic region. The predicted results of the model are in good agreement with the results of field observations, as shown in Figure 16. Because the model does not need complex calibration experiments and the model parameters are universal, the fluctuating velocity prediction model is easy to apply.

5. Electric Field Measurements in Dust Storms

Particle charging is a ubiquitous phenomenon in industry (e.g. fluidized beds (Sippola et al. 2018)), nature (e.g. volcanic eruptions and dust storms (Mather & Harrison, 2006; Zhang & Zhou, 2020b)), and even interplanetary and interstellar space (e.g. protoplanetary disks and dusty plasmas (Blum & Wurm 2008)). Dust storms are natural laboratories for the study of particle charging in particle-laden turbulent flows, with friction Reynolds numbers reaching as high as $Re_\tau \sim O(10^6)$, and dust storms containing polydisperse sand and dust particles ranging in size from $O(10^{-6})$ to $O(10^{-3})$ m. The ambient electric field density in dust storms reaches $\sim 10\text{--}100$ kV m^{-1} , which is 2–3 orders of magnitude higher than that of the fair-weather atmospheric electric field (e.g. Harris, 1967; Kamra, 1972; Rudge, 1913; Stow, 1969; Zhang & Zhou, 2020b). Numerous studies have shown that the electrostatic forces to which particles are

subjected are comparable to their gravitational force, which has considerable influences on the particle lifting process, preferential particle concentration, and particle transport (e.g. Kok & Renno, 2006; Renzo & Urzay, 2018; Schmidt, Schmidt, & Dent, 1998; Zheng, Huang, & Zhou, 2003). For example, Kok and Renno (2006) showed that electrostatic forces between particles can significantly reduce the critical wind speed for particle lifting and even directly lift particles away from the wall. Renzo and Urzay (2018) conducted numerical simulations and discovered that electrostatic forces can remarkably affect the preferential concentration of particles in turbulent flows. Zheng et al. (2003) showed that in wind-blown sand flows, the electrostatic force increases the dust mass flux when the dust particles are negatively charged, while the electrostatic force decreases the dust mass flux when the dust particles are positively charged. In addition, the theoretical model of Zhou, He, and Zheng (2005) shows that the transmission of electromagnetic waves in dust storms is significantly affected by the amount of electrical charge on the dust particles.

The electrostatic force exerted on a dust particle is equal to the product of the particles' charge-to-mass ratio and the electric field strength at its spatial location; hence, the particles' charge-to-mass ratio and the spatial structure of the electric field are two important physical quantities for quantifying the particle charging phenomena in dust storms. Currently, two methods, namely, the trajectory deflection method (e.g. Miura, Koyaguchi, & Tanaka, 2002) and the Faraday cage method (e.g. Schmidt et al., 1998), are employed to measure the charge-to-mass ratio of particles. The former method indirectly determines the particles' charge-to-mass ratio by measuring the horizontal deflection of the trajectory of the charged particles under an applied horizontal electric field, and the magnitude of this horizontal deflection is proportional to the particles' charge-to-mass ratio; however, as the accuracy of this method depends on the precise measurement of particle trajectories (usually using PIV, e.g. Waitukaitis, Lee, Pierson, Forman, & Jaeger, 2014), it cannot be used for dust storm measurements. The latter method determines the average charge-to-mass ratio of particles during a period by measuring the total charge and mass of the particles collected in a Faraday cage in real time. This method has been widely used to measure the charge-to-mass ratios of sand and dust particles (e.g. Bo, Zhang, & Zheng, 2014; Schmidt et al., 1998) within the saltation layer (i.e. within a height of ~ 10 cm above the surface). However, it is difficult to apply this method at higher altitudes, where the particle concentration is small and the wind shear stress is strong enough that particles can hardly be collected in a Faraday cage (e.g. Harrison et al., 2016). Therefore, the electrical properties of suspended dust particles in dust storms are currently unclear, and the particles' charge-to-mass ratio is usually assumed to be a constant of $\sim \pm 60 \mu\text{C kg}^{-1}$ in many numerical models (e.g. Schmidt et al., 1998; Zhang & Zhou, 2020a; Zheng et al., 2003); this magnitude is consistent with the measurements of (Schmidt et al., 1998). Although Williams, Nathou, Hicks, Pontikis, and Bartholomew (2009) inferred that the charge structure of dust storms may be unipolar or bipolar (if particle charging occurs primarily at the ground or in midair, respectively), they neglected the effects of turbulence, which plays an important role in particle charging (e.g. Grosshans & Papalexandris, 2017; Renzo & Urzay, 2018). Consequently, they did not obtain detailed information about the electrical properties of the suspended particles.

On the other hand, although Rudge (1913) conducted observations of atmospheric electric field changes during dust storms as early as 1913, the spatial structure of the aeolian electric field during a dust storm remains puzzling owing to its complexity (Harrison et al., 2016; Zheng, 2013). As shown in Figure 17, the existing observations of the aeolian electric field are concerned mainly with the vertical component, and these measurements were performed at a single point $\sim 1\text{--}2$ m above the ground (Esposito, 2016; Harris, 1967; Kamra, 1972; Rudge, 1913; Stow, 1969; Yair, Katz, Yaniv, Ziv, & Price, 2016); thus, the spatial structure of the aeolian electric field was not retrieved. In particular, the direction of the vertical component of the aeolian electric field is still under debate. That is, measurements have uncovered upward-oriented (e.g. Harris, 1967; Rudge, 1913; Stow, 1969), downward-oriented (e.g. Esposito, 2016), and even alternatively oriented vertical electric fields (Kamra, 1972; Williams et al., 2009).

To obtain the electrical properties of the suspended particles at high altitudes and image the fine structure of the electric field in dust storms, a set of real-time, simultaneous, multipoint observations

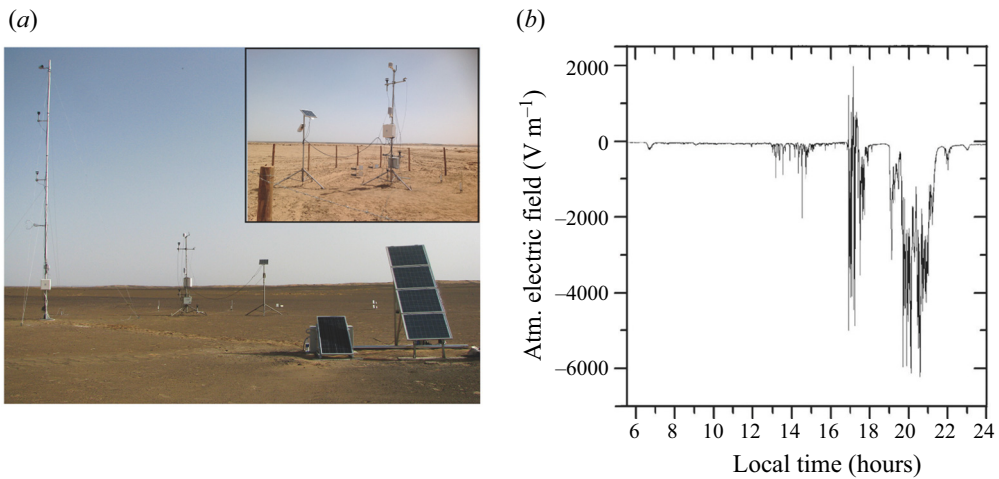


Figure 17. Field observations of the aeolian electric field in dust storms by *Esposito et al. (2016)*. (a) Instrument stations deployed in the field observations, which were conducted in the Merzouga Desert, Morocco in 2014. The inset shows the installation of the instruments in 2013. (b) Time series of the vertical electric field at a height of 2 m measured on 16 July 2013. The positive direction of the vertical electric field is oriented upward. This figure was adapted from *Esposito et al. (2016)*.

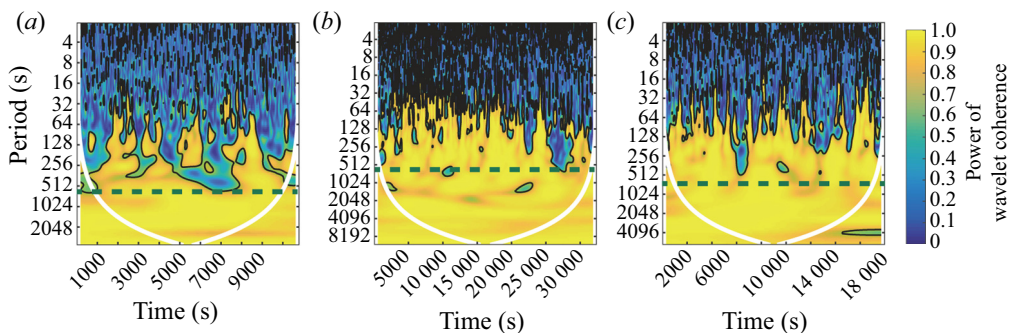


Figure 18. Wavelet coherence between the space charge density (estimated from the divergence of the three-dimensional electric field measurements) and the PM10 dust mass concentration at a measurement point 5 m above the ground. Panels (a–c) correspond to dust storms observed on 17 April, 20 April and 22 April 2017, respectively. The horizontal dashed line corresponds to a time scale of 10 min and the white solid line is the cone of influence for wavelet analysis. This figure was adapted from *Zhang and Zheng (2018)*.

of the wind velocity, PM10 dust concentration and electric field were performed at the QLOA (*Zhang, Bo, & Zheng, 2017; Zhang & Zhou, 2020b*). First, as shown in *Figure 18*, the space charge density and dust mass concentration 5 m above the ground are weakly correlated at short time scales (i.e. <1 min), while they show a highly linear correlation (wavelet coherence ≥ 0.8) at long time scales (exceeding 10 min) at different stages of the dust storm. Because the ratio of the space charge density to the dust mass concentration characterizes the average charge-to-mass ratio of the suspended particles, a strong correlation at a time scale exceeding 10 min indicates that the average charge-to-mass ratio does not change with the dust concentration over this scale. Such a strong correlation is usually termed the large-scale electrification equilibrium phenomenon of dust particles in dust storms (e.g. *Harper & Dufek, 2016; Zhang & Zheng, 2018*). *Zhang and Zheng (2018)* showed that for a given ambient temperature and

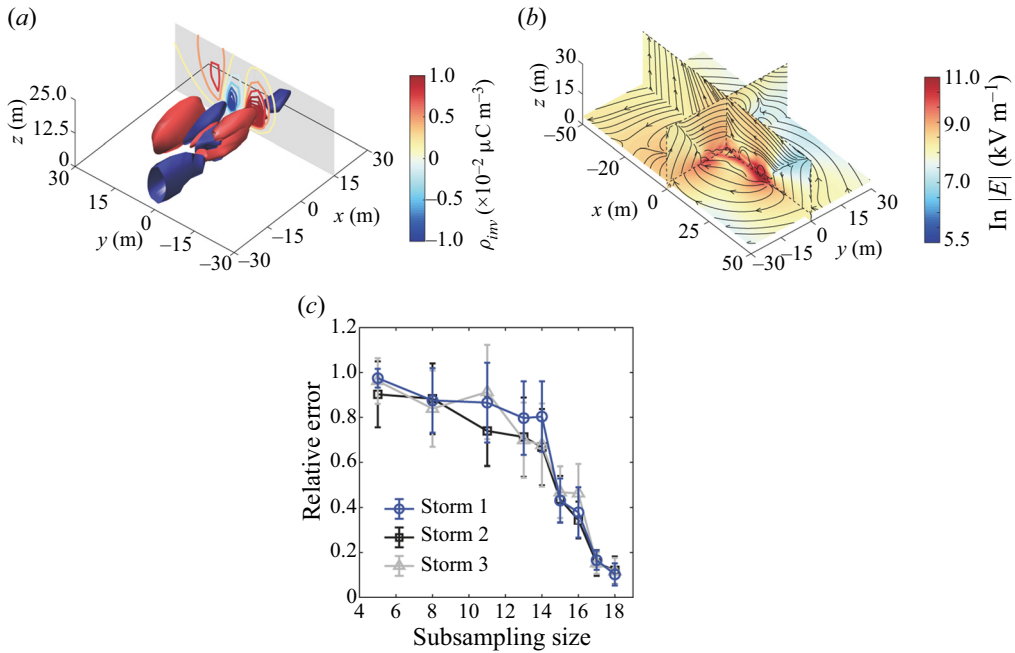


Figure 19. Reconstruction of the electrical structure of a dust storm, where the electric field data are from observations collected on 16 April 2017 at 13:20:00 (UTC+8). (a) Reconstruction of the three-dimensional structure of the space charge density ρ_{inv} on 16 April 2017 at 13:20:00 (UTC+8), where the isosurfaces are shown at a space charge density magnitude of $0.02 \mu\text{C m}^{-3}$. The positive and negative surfaces are coloured red and blue, respectively. Contour slices at $x = 5 \text{ m}$ are coloured based on the space charge densities. (b) Reconstruction of the three-dimensional structure of the electric field on 16 April 2017 at 13:20:00 (UTC+8), where the lines are electric field lines and the contour clouds are stained with the logarithm of the electric field size. Slices at $x = 0$, $y = 0$ and $z = 4 \text{ m}$ are coloured based on the log magnitude of the three-dimensional electric field. (c) Relative error between the ρ_{inv} obtained from the reconstructions with subsampling and complete sampling, where the subsampling size m ranges from 5 to 18 for the three different data sets of dust storms 1–3. Dust storms 1, 2 and 3 occurred on 16, 17, and 20 April 2017 (UTC+8), respectively. Error bars represent the standard deviation of the relative error over 10 random subsampling reconstructions. This figure was adapted from Zhang and Zhou (2020b).

relative humidity, there is a significant fluctuation in the average charge-to-mass ratio below the 10 min scale, while the average charge-to-mass ratio is considered to remain unchanged above the 10 min scale.

Furthermore, Zhang and Zhou (2020b) employed Tikhonov regularization and proposed a method to reconstruct the spatial structures of the space charge density and electric field in dust storms based on locally measured electric field data in the ASL, thereby providing a method for studying the electrical structure of dust storms. The reconstructed results in Figure 19a indicate that the space charge density in dust storms exhibits a universal mosaic pattern (i.e. a mosaic of positively and negatively charged regions), which implies that the charge-to-mass ratio of dust particles varies spatially. Surprisingly, this mosaic charge structure is quite different from the unipolar or bipolar charge structures inferred from previous work (Williams et al., 2009). This is because particle charging is generally size-dependent; i.e. large particles tend to be positively charged, whereas small particles tend to be negatively charged (Lacks & Sankaran, 2011). In dust storms, negatively charged small particles with an S_t (Stokes) number less than $\sim O(1)$ accumulate in the low-speed region owing to turbulence, while particles with an S_t number much larger than $\sim O(1)$ are distributed more uniformly owing to their large inertia (Lacks &

Sankaran, 2011). It is likely that these different responses of charged particles to turbulence are the main physical mechanism that generates the mosaic charge structure of dust storms (e.g. Cimarelli, Alatorre-Ibarguengoitia, Kueppers, Scheu, & Dingwell, 2014; Renzo & Urzay, 2018). Moreover, as shown in Figure 19b, the electric field of the dust storms is three-dimensional at different locations. Therefore, field measurements should focus on the three-dimensional electric field and not only on the vertical component. Note that the measurement points in the streamwise direction play an important role in the reconstruction model. As shown in Figure 19c, the relative error between the subsampling and complete sample reconstructions reaches 40 % when the streamwise measurement points (i.e. streamwise towers 5 m above the ground) have been removed. This means that such subsampling reconstructions are unreliable. In fact, because the space charge density in a dust storm is not uniformly distributed in the streamwise direction, a reconstruction with insufficient streamwise data cannot fully reproduce the real structures.

6. Conclusion and Outlook

Wind-blown sand flows/sandstorms are typical gas–solid two-phase flows that not only constitute frontier foundational science issues but also present significant application requirements for studying their regularity and formation/evolutionary mechanisms. However, it is difficult to study high-Reynolds-number two-phase wall-bounded turbulence owing to the lack of existing research methods; consequently, the understanding of such flows remains poor. As discussed in this paper, based on a review and summary of the current research status on LSMs/VLSMs in high-Reynolds-number wall-bounded turbulence, the innovative results reported in this field are focused primarily on the observations of wind-blown sand-laden two-phase flows in the ASL, especially the results obtained from the QLOA. These research successes mainly include: discovering the existence of VLSMs in the flow field and very-large-scale sand structures in the sand concentration scalar field in high-Reynolds-number particle-laden flows ($Re_\tau \sim O(10^6)$); ascertaining the scale, structure inclination angle and other features of VLSMs in the particle-laden ASL flow; determining the energy distribution with height and its difference between particle-laden and particle-free flows; the effects of sand particles on the amplitude modulation effect between multiscale turbulent motions; further modifying Taylor's hypothesis of frozen turbulence based on the difference between the streamwise scales of the VLSMs measured by the streamwise array and the corresponding results obtained by this hypothesis; and retrieving the space charge density and electric field of a sandstorm from spatial multipoint three-dimensional electric field synchronous measurements. These theories provide guidance for predicting wind-blown sand flows in the ASL, especially for improving the sand flux model based on the steady flow field and stationary saltation hypothesis, and for studying the physics of wind-blown sand movement (Anderson & Haff, 1988; McEwan & Willetts, 1991).

Based on the understanding of the phenomena and mechanisms discussed herein revealed by the existing research on high-Reynolds-number wall-bounded turbulence and wind-blown sand-laden two-phase flows, the author summarizes the following key issues that need to be further studied.

1. The coupling effects between near-wall motions of particles and turbulence. An erodible surface can be found in wind-blown sand flows/sandstorms. The motions of near-wall particles, especially heavy particles, such as sand, include impacts/collisions, rebounding/splashing and creeping/saltating on an erodible surface. Moreover, the near-wall turbulent motions include hairpin vortices, streaks, ejection and sweep events, and LSMs/VLSMs. The coupling effect between these two types of near-wall motions and their influence on turbulence structures can play key roles in the formation and evolution of gas–solid two-phase flows, especially turbulence structures, as well as significantly complicate the occurrence of two-phase particle-laden wall turbulence. Therefore, quantitatively characterizing the coupling effect between these two types of near-wall motions and their influencing mechanism can enhance the understanding of the evolutionary characteristics of turbulence structures and improve the prediction of gas–solid two-phase flows, especially wind-blown sand flows/sandstorms, in terms of accuracy and precision.

2. The particle concentration effects on the statistics and VLSM characteristics in high-Reynolds-number particle-laden turbulence. In current studies, both the turbulence statistics (such as the mean wind profile, turbulence fluctuation intensity and Reynolds shear stress) and the VLSM characteristics (including the scale, structure inclination angle, energy fraction and amplitude modulation) are significantly affected by the existence of sand particles in wind-blown sand-laden two-phase flows. However, most of these statistics are limited in their qualitative differences from the comparison of particle-laden and particle-free results. Therefore, studies on the turbulence statistics and structural characteristics that vary with different concentrations of sand particles are lacking. Future research on this topic will need to realize the synchronous measurement of the near-wall wind velocity and the concentration of particles (especially with a larger particle concentration in the ASL, which is much more difficult to measure).

3. The research methods in high-Reynolds-number gas–solid two-phase flows. The research methods used to investigate gas–solid two-phase flows are mainly experiments and numerical simulations, where the former includes field observations and wind tunnel experiments. However, owing to uncontrollable environmental factors and the surface conditions of field observations, near-wall measurements are difficult to perform in the saltation layer of a wind-blown sand-laden two-phase flow. Moreover, wind tunnel experiments performed on gas–solid two-phase flows under controlled conditions cannot satisfy the complete measurement of VLSMs owing to the limited field of view of PIV. With regard to numerical simulations, real wind-blown sand flows/sandstorms have a higher Reynolds number ($Re_\tau \sim O(10^6)$) and density ratio (the particle-to-fluid density ratio is approximately 2000), an obvious gravity settlement process and strong near-wall motions of particles on the erodible surface, and multiscale motions and scale-spanning motions are coupled simultaneously. Therefore, while the Reynolds numbers of full-resolution DNSs of particles and turbulence are being continuously improved, the influences of gravity and the erodible surface should be considered, and a scale-spanning high-precision numerical algorithm needs to be developed from the near-wall motion of a single particle to the motions of a particle swarm and the transport of particles from near the wall to the middle of the ASL.

4. The evolution of turbulence properties and structural characteristics during sandstorms. According to changes in the wind velocity, the whole process of a sandstorm can be divided into three sections: a rising stage with increasing wind velocity, a stationary stage with stable wind velocity and a declining stage with decreasing wind velocity. Existing wind-blown sand-laden two-phase flow studies focus on analysing only the stationary process. In contrast, investigating the turbulence statistical properties, especially the evolutionary regularities of the structural characteristics over time, throughout the whole sandstorm process, which includes the rising and descending stages, would be helpful to reveal the mechanisms of sandstorm formation and evolution, and therefore achieve the effective control of sandstorms. However, relevant research has yet to be reported, so further experimental observations, as well as the development of reliable non-stationary data processing methods suitable for the rising and declining stages of sandstorms, are needed.

5. The structures of the three-dimensional electric field and dust concentration field in dust storms. The mosaic charge structure arising from the different responses of oppositely charged particles to turbulence in dust storms implies that the electrical structure of dust storms is closely related to the structure of the turbulent flows. Therefore, a joint reconstruction model for reconstructing the turbulent flows, dust concentration field and electric field is needed to reveal the coupling mechanisms among them. Additionally, because almost all the existing studies are concerned mainly with the properties of the mean electric field, the fluctuating properties of the aeolian electric field remain largely unknown. Future research should focus on the statistical quantities of the fluctuating field, such as the power spectra of fluctuating electric fields and the coherence spectra among the fluctuating electric field, dust concentration and turbulence, from which the energy distribution and coherence can be assessed across different scales.

6. The application of research achievements on high-Reynolds-number gas–solid two-phase flows. The flows in nature and industrial applications are mostly multiphase flows with high Reynolds numbers. For sandstorms, wind-blown sand flows and the diffusion of pollutants, the transport of particles should be limited through the study of particle two-phase flows. However, for industrial applications, such as

coal combustion and pneumatic transport, particles and fluids must be fully mixed. Therefore, based on the deep understanding of the regularities and physical mechanisms of the interactions between particles and turbulence, it is necessary to establish a theoretical framework and prediction method that are suitable for high-Reynolds-number gas–solid two-phase wall-bounded turbulent flows to better realize the advantages and disadvantages of particle-laden two-phase flows.

Acknowledgements. We gratefully acknowledge the support of coworkers for the figures and data cited in this manuscript. The authors would like to express their sincere appreciation for the support.

Funding Statement. The authors gratefully acknowledge funding from the National Natural Science Foundation of China (92052202 and 11802110).

Declaration of Interests. The authors report no conflict of interest.

Author Contributions. X.Z. proposed the research plan, designed the review frame and carefully modified the manuscript. H.L. wrote the manuscript.

Data Availability Statement. Raw data are available from the corresponding author (X.Z.).

Ethical Standards. The review article meets all ethical guidelines, including adherence to the legal requirements of the study country.

References

- Adrian, R. J., Meinart, C. D., & Tomkins, C. D. (2000). Vortex organization in the outer region of the turbulent boundary layer. *Journal of Fluid Mechanics*, *422*, 1–54.
- Ahn, J., Lee, J. H., Lee, J., Kang, J. H., & Sung, H. J. (2015). Direct numerical simulation of a 30R long turbulent pipe flow at $Re_\tau = 3008$. *Physics of Fluids*, *27*, 14.
- Anderson, R. S., & Haff, P. K. (1988). Simulation of eolian saltation. *Science*, *241*, 820–823.
- Anderson, W. (2016). Amplitude modulation of streamwise velocity fluctuations in the roughness sublayer: Evidence from large-eddy simulations. *Journal of Fluid Mechanics*, *789*, 567–588.
- Baars, W. J., Hutchins, N., & Marusic, I. (2016). Spectral stochastic estimation of high-Reynolds-number wall-bounded turbulence for a refined inner-outer interaction model. *Physical Review Fluids*, *1*(5), 054406.
- Bagnold, R. A. (1941). *The physics of blown sand and desert dunes*. London: Methuen.
- Balachandar, S., & Eaton, J. K. (2010). Turbulent dispersed multiphase flow. *Annual Review of Fluid Mechanics*, *42*(1), 111–133.
- Balakumar, B. J., & Adrian, R. J. (2007). Large- and very-large-scale motions in channel and boundary-layer flows. *Philosophical Transactions of the Royal Society of London A: Mathematical, Physical and Engineering Sciences*, *365*(1852), 665–681.
- Bandyopadhyay, P. R., & Hussain, A. K. M. F. (1984). The coupling between scales in shear flows. *Physics of Fluids*, *27*(9), 2221–2228.
- Barad, M. L. (1964). The vertical transfer of momentum and heat at and near the earth's surface. *Transactions New York Academy of Sciences*, *26*(7 Series II), 830–844.
- Berk, T., & Coletti, F. (2020). Transport of inertial particles in high-Reynolds-number turbulent boundary layers. *Journal of Fluid Mechanics*, *903*, A18.
- Blackwelder, R. F., & Kovaszny, L. S. (1972). Time scales and correlations in a turbulent boundary layer. *Physics of Fluids*, *15*, 1545–1554.
- Blum, J., & Wurm, G. (2008). The growth mechanisms of macroscopic bodies in protoplanetary disks. *Annual Review of Astronomy and Astrophysics*, *46*, 21–56.
- Bo, T. L., Zhang, H., & Zheng, X. J. (2014). Charge-to-mass ratio of saltating particles in wind-blown sand. *Scientific Reports*, *4*, 5590.
- Boppe, R. S., & Neu, W. L. (1995). Quasi coherent structures in the marine atmospheric surface layer. *Journal of Geophysical Research: Oceans*, *100*(C10), 20635–20648.
- Boppe, R. S., & Neu, W. L. (1999). Large-scale motions in the marine atmospheric surface layer. *Boundary-Layer Meteorology*, *92*(2), 165–183.
- Brown, G. L., & Thomas, A. S. (1977). Large structure in a turbulent boundary layer. *Physics of Fluids*, *20*(10), S243–S252.
- Carper, M. A., & Porté-Agel, F. (2004). The role of coherent structures in subfilter-scale dissipation of turbulence measured in the atmospheric surface layer. *Journal of Turbulence*, *5*, 32–32.
- Chauhan, K., Hutchins, N., Monty, J., & Marusic, I. (2013). Structure inclination angles in the convective atmospheric surface layer. *Boundary-Layer Meteorology*, *147*(1), 41–50.
- Choi, H., & Moin, P. (2012). Grid-point requirement for large eddy simulation: Chapman's estimation revisited. *Physics of Fluids*, *24*, 011702.
- Christensen, K. T., & Adrian, R. J. (2001). Statistical evidence of hairpin vortex packets in wall turbulence. *Journal of Fluid Mechanics*, *431*, 433–443.

- Cimarelli, C., Alatorre-Ibarguengoitia, M. A., Kueppers, U., Scheu, B., & Dingwell, D. B. (2014). Experimental generation of volcanic lightning. *Geology*, *42*, 79–82.
- Cooper, D. I., Leclerc, M. Y., Archuleta, J., Coulter, R., Eichinger, W. E., Kao, C. Y. J., & Nappo, C. J. (2006). Mass exchange in the stable boundary layer by coherent structures. *Agricultural & Forest Meteorology*, *136*, 114–131.
- Corsin, S., & Kistler, A. L. (1954). Free-stream boundaries of turbulent flows. *NACA Technical Note*, 3133.
- Deck, S., Renard, N., Laraufe, R., & Weiss, P.-É. (2014). Large-scale contribution to mean wall shear stress in high-Reynolds-number flat-plate boundary layers up to $Re_\theta = 13\,650$. *Journal of Fluid Mechanics*, *743*, 202–248.
- Deng, B. Q., Huang, W. X., & Xu, C. X. (2016). Origin of effectiveness degradation in active drag reduction control of turbulent channel flow at $Re_\tau = 1000$. *Journal of Turbulence*, *17*, 758–786.
- Dennis, D. J. (2015). Coherent structures in wall-bounded turbulence. *Anais da Academia Brasileira de Ciências*, *87*(2), 1161–1193.
- Elghobashi, S. (1994). On predicting particle-laden turbulent flows. *Applied Scientific Research*, *52*, 309–329.
- Esposito, F. (2016). The role of the atmospheric electric field in the dust lifting process. *Geophysical Research Letters*, *43*, 5501–5508.
- Esposito, F., Molinaro, R., Popa, C. I., Molfese, C., Cozzolino, F., Marty, L., Taj-Eddine, K., Di Achille, G., Franzese, G., Silvestro, S., & Ori, G. G. (2016). The role of the atmospheric electric field in the dust lifting process. *Geophysical Research Letters*, *43*, 5501–5508.
- Falco, R. E. (1977). Coherent motions in the outer region of turbulent boundary layers. *Physics of Fluids (1958–1988)*, *20*(10), S124–S132.
- Ganapathisubramani, B., Hutchins, N., Hambleton, W. T., Longmire, E. K., & Marusic, I. (2005). Investigation of large-scale coherence in a turbulent boundary layer using two-point correlations. *Journal of Fluid Mechanics*, *524*, 57–80.
- Grant, H. L. (1958). The large eddies of turbulent motion. *Journal of Fluid Mechanics*, *4*(02), 149–190.
- Grosshans, H., & Papalexandris, M. V. (2017). Direct numerical simulation of triboelectric charging in particle-laden turbulent channel flows. *Journal of Fluid Mechanics*, *818*, 465–491.
- Gu, H., Wang, G., Zhu, W., & Zheng, X. J. (2019). Gusty wind disturbances & large-scale turbulent structures in the neutral atmospheric surface layer. *Science China Physics, Mechanics & Astronomy*, *62*, 114711.
- Guala, M., Hommema, S. E., & Adrian, R. J. (2006). Large-scale and very-large-scale motions in turbulent pipe flow. *Journal of Fluid Mechanics*, *554*, 521–542.
- Guala, M., Metzger, M., & McKeon, B. J. (2011). Interactions within the turbulent boundary layer at high Reynolds number. *Journal of Fluid Mechanics*, *666*, 573–604.
- Han, G., Liu, L., Bo, T., & Zheng, X. (2019). A predictive model for the streamwise velocity in the near-neutral atmospheric surface layer. *Journal of Geophysical Research-Atmospheres*, *124*, 238–251.
- Han, G., Wang, G., & Zheng, X. (2019). The applicability of Taylor's hypothesis for estimating the mean streamwise length scales of large-scale structures in the near-neutral atmospheric surface layer. *Boundary-Layer Meteorology*, *172*, 215–237.
- Harper, J. M., & Dufek, J. (2016). The effects of dynamics on the triboelectrification of volcanic ash. *Journal of Geophysical Research Atmospheres*, *121*(14), 8209–8228.
- Harris, D. J. (1967). Electrical effects of the Harmattan dust storms. *Nature*, *214*, 585.
- Harrison, R. G., Barth, E., Esposito, F., Merrison, J., Montmessin, F., Aplin, K. L., . . . Farrell, W. M. (2016). Applications of electrified dust and dust devil electrostatics to Martian atmospheric electricity. *Space Science Reviews*, *203*, 299–345.
- He, G., Jin, G., & Yang, Y. (2017). Space-time correlations & dynamic coupling in turbulent flows. *Annual Review of Fluid Mechanics*, *49*, 51–70.
- Head, M. R., & Bandyopadhyay, P. (1981). New aspects of turbulent boundary-layer structure. *Journal of Fluid Mechanics*, *107*, 297–338.
- Heisel, M., Dasari, T., Liu, Y., Hong, J., Coletti, F., & Guala, M. (2018). The spatial structure of the logarithmic region in very-high-Reynolds-number rough wall turbulent boundary layers. *Journal of Fluid Mechanics*, *857*, 704–747.
- Hommema, S. E., & Adrian, R. J. (2003). Packet structure of surface eddies in the atmospheric boundary layer. *Boundary-Layer Meteorology*, *106*(1), 147–170.
- Hong, J., Toloui, M., Chamorro, L. P., Guala, M., Howard, K., Riley, S., . . . Sotiropoulos, F. (2014). Natural snowfall reveals large-scale flow structures in the wake of a 2.5-MW wind turbine. *Nature Communications*, *5*, 4216.
- Horiguchi, M., Hayashi, T., Adachi, A., & Onogi, S. (2012). Large-scale turbulence structures & their contributions to the momentum flux & turbulence in the near-neutral atmospheric boundary layer observed from a 213 m tall meteorological tower. *Boundary-Layer Meteorology*, *144*, 179–198.
- Howland, M. F., & Yang, X. I. A. (2018). Dependence of small-scale energetics on large scales in turbulent flows. *Journal of Fluid Mechanics*, *852*, 641–662.
- Hoyas, S., Oberlack, M., Kraheberger, S., & Alcantara-Avila, F. (2018). Turbulent channel flow at $Re_\tau = 10\,000$. In *APS Division of Fluid Dynamics Meeting*. Nov. 18–20, Atlanta, USA.
- Hutchins, N., Chauhan, K., Marusic, I., Monty, J., & Klewicki, J. (2012). Towards reconciling the structure of boundary layers in the atmosphere and laboratory. *Boundary-Layer Meteorology*, *145*, 273–306.
- Hutchins, N., Hambleton, W. T., & Marusic, I. (2005). Inclined cross-stream stereo particle image velocimetry measurements in turbulent boundary layers. *Journal of Fluid Mechanics*, *541*, 21–54.

- Hutchins, N., & Marusic, I. (2007a). Evidence of very long meandering features in the logarithmic region of turbulent boundary layers. *Journal of Fluid Mechanics*, 579, 1–28.
- Hutchins, N., & Marusic, I. (2007b). Large-scale influences in near-wall turbulence. *Philosophical Transactions of the Royal Society of London A: Mathematical, Physical and Engineering Sciences*, 365(1852), 647–664.
- Hwang, J., & Sung, H. J. (2017). Influence of large-scale motions on the frictional drag in a turbulent boundary layer. *Journal of Fluid Mechanics*, 829, 751–779.
- Inoue, M., Mathis, R., Marusic, I., & Pullin, D. I. (2012). Wall shear-stress statistics for the turbulent boundary layer by use of a predictive wall-model with LES. In *Proceedings of the 18th Australasian Fluid Mech. Conference*. Launceston, Australia.
- Jacob, C., & Anderson, W. (2017). Conditionally averaged large-scale motions in the neutral atmospheric boundary layer: Insights for aeolian processes. *Boundary-Layer Meteorology*, 162(1), 1–21.
- Jacobi, I., & Mckeon, B. J. (2013). Phase relationships between large and small scales in the turbulent boundary layer. *Experiments in Fluids*, 54(3), 1481.
- Ji, C., Munjiza, A., Avital, E., Xu, D., & Williams, J. (2014). Saltation of particles in turbulent channel flow. *Physical Review E*, 89, 052202.
- Jiménez, J. (2013). Near-wall turbulence. *Physics of Fluids*, 25, 101302.
- Jiménez, J., & Pinelli, A. (1999). The autonomous cycle of near-wall turbulence. *Journal of Fluid Mechanics*, 389, 335–359.
- Kaimal, J. C., & Wyngaard, J. C. (1989). The Kansas & Minnesota experiments. *Boundary-Layer Meteorology*, 50, 31–47.
- Kamra, A. K. (1972). Measurements of the electrical properties of dust storms. *Journal of Geophysical Research*, 77, 5856–5869.
- Katul, G., & Vidakovic, B. (1996). The partitioning of attached and detached eddy motion in the atmospheric surface layer using Lorentz wavelet filtering. *Boundary-Layer Meteorology*, 77, 153–172.
- Khalitov, D. A., & Longmire, E. K. (2002). Simultaneous two-phase PIV by two-parameter phase discrimination. *Experiments in Fluids*, 32, 252–268.
- Kim, K. C., & Adrian, R. J. (1999). Very large-scale motion in the outer layer. *Physics of Fluids*, 11(2), 417–422.
- Klewicki, J. C., Fife, P., & Wei, T. (2009). On the logarithmic mean profile. *Journal of Fluid Mechanics*, 638, 73–93.
- Kok, J. F., & Renno, N. O. (2006). Enhancement of the emission of mineral dust aerosols by electric forces. *Geophysical Research Letters*, 33, L19S10.
- Kovaszny, L. S. G., Kibens, V., & Blackwelder, R. F. (1970). Large-scale motion in the intermittent region of a turbulent boundary layer. *Journal of Fluid Mechanics*, 41(2), 283–325.
- Krogstad, P. Å., & Antonia, R. A. (1994). Structure of turbulent boundary layers on smooth and rough walls. *Journal of Fluid Mechanics*, 277, 1–21.
- Kulick, J. D., Fessler, J. R., & Eaton, J. K. (1994). Particle response and turbulence modification in fully developed channel flow. *Journal of Fluid Mechanics*, 277, 109–134.
- Kunkel, G. J., & Marusic, I. (2006). Study of the near-wall-turbulent region of the high-Reynolds-number boundary layer using an atmospheric flow. *Journal of Fluid Mechanics*, 548, 375–402.
- Lacks, D. J., & Sankaran, R. M. (2011). Contact electrification of insulating materials. *Journal of Physics D Applied Physics*, 44, 453001.
- Lee, J. H., & Sung, H. J. (2011). Very-large-scale motions in a turbulent boundary layer. *Journal of Fluid Mechanics*, 673, 80–120.
- Lesieur, M., & Métais, O. (1996). New trends in large-eddy simulations of turbulence. *Annual Review of Fluid Mechanics*, 28(1), 45–82.
- Li, B., & Neuman, C. M. (2012). Boundary-layer turbulence characteristics during aeolian saltation. *Geophysical Research Letters*, 39, L11402.
- Liu, H. Y., Bo, T. L., & Liang, Y. R. (2017). The variation of large-scale structure inclination angles in high Reynolds number atmospheric surface layers. *Physics of Fluids*, 29(3), 035104.
- Liu, H. Y., Wang, G. H., & Zheng, X. J. (2017). Spatial length scales of large-scale structures in atmospheric surface layers. *Journal of Fluid Mechanics*, 2(6), 064606.
- Liu, H. Y., Wang, G. H., & Zheng, X. J. (2019a). Three-dimensional representation of large-scale structures based on observations in atmospheric surface layers. *Journal of Geophysical Research: Atmospheres*, 124, 10753–10771.
- Liu, H. Y., Wang, G. H., & Zheng, X. J. (2019b). Amplitude modulation between multi-scale turbulent motions in high-Reynolds-number atmospheric surface layers. *Journal of Fluid Mechanics*, 861, 858–607.
- Liu, H. Y., & Zheng, X. J. (2020). Amplitude modulation in particle-laden atmospheric surface layers. *Journal of Fluid Mechanics*, submitted.
- Luhar, M., Sharma, A. S., & McKeon, B. J. (2014). On the structure and origin of pressure fluctuations in wall turbulence: predictions based on the resolvent analysis. *Journal of Fluid Mechanics*, 751, 38–70.
- Martin, R. L., & Kok, J. F. (2018). Distinct thresholds for the initiation & cessation of aeolian saltation from field measurements. *Journal of Geophysical Research: Earth Surface*, 123(7), 1546–1565.
- Marusic, I., & Heuer, W. D. (2007). Reynolds number invariance of the structure inclination angle in wall turbulence. *Physical Review Letters*, 99(11), 114504.
- Marusic, I., & Hutchins, N. (2008). Study of the log-layer structure in wall turbulence over a very large range of Reynolds number. *Flow, Turbulence and Combustion*, 81(1–2), 115–130.
- Marusic, I., & Hutchins, N. (2011). A wall-shear stress predictive model. *Journal of Physics: Conference Series*, 318(1), 012003.

- Marusic, I., Kunkel, G. J., & Porte-Agel, F. (2001). Experimental study of wall boundary conditions for large-eddy simulation. *Journal of Fluid Mechanics*, 446, 309–320.
- Marusic, I., Mathis, R., & Hutchins, N. (2010). Predictive model for wall-bounded turbulent flow. *Science*, 329(5988), 193–196.
- Marusic, I., McKeon, B. J., Monkewitz, P. A., Nagib, H. M., Smits, A. J., & Sreenivasan, K. R. (2010). Wall-bounded turbulent flows at high Reynolds numbers: Recent advances and key issues. *Physics of Fluids*, 22(6), 065103.
- Marusic, I., & Monty, J. P. (2019). Attached eddy model of wall turbulence. *Annual Review of Fluid Mechanics*, 51, 49–74.
- Marusic, I., Monty, J. P., Hultmark, M., & Smits, A. J. (2013). On the logarithmic region in wall turbulence. *Journal of Fluid Mechanics*, 716, R3.
- Mather, T. A., & Harrison, R. G. (2006). Electrification of volcanic plumes. *Surveys in Geophysics*, 27(4), 387–432.
- Mathis, R., Hutchins, N., & Marusic, I. (2009). Large-scale amplitude modulation of the small-scale structures in turbulent boundary layers. *Journal of Fluid Mechanics*, 628, 311–337.
- Mathis, R., Hutchins, N., & Marusic, I. (2011). A predictive inner-outer model for streamwise turbulence statistics in wall-bounded flows. *Journal of Fluid Mechanics*, 681, 537–566.
- Mathis, R., Marusic, I., Chernyshenko, S. I., & Hutchins, N. (2013). Estimating wall-shear-stress fluctuations given an outer region input. *Journal of Fluid Mechanics*, 715, 163–180.
- Mathis, R., Monty, J., Hutchins, N., & Marusic, I. (2009). Comparison of large-scale amplitude modulation in turbulent boundary layers, pipes, and channel flows. *Physics of Fluids*, 21, 111703.
- McEwan, I. K., & Willetts, B. B. (1991). Numerical model of the saltation cloud. *Aeolian Grain Transport 1. Acta Mechanica Supplementum*, pp. 53–66.
- Meneveau, C., & Katz, J. (2000). Scale-invariance and turbulence models for large-eddy simulation. *Annual Review of Fluid Mechanics*, 32(1), 1–32.
- Metzger, M. M. (2002). *Scalar dispersion in high Reynolds number boundary layers* (PhD dissertation). University of Utah.
- Metzger, M. M., & Klewicki, J. C. (2001). A comparative study of near-wall turbulence in high and low Reynolds number boundary layers. *Physics of Fluids*, 13(3), 692–701.
- Miura, T., Koyaguchi, T., & Tanaka, Y. (2002). Measurements of electric charge distribution in volcanic plumes at Sakurajima Volcano, Japan. *Bulletin of Volcanology*, 64(2), 75–93.
- Moin, P., & Kim, J. (1982). Numerical investigation of turbulent channel flow. *Journal of Fluid Mechanics*, 118, 341–377.
- Mola, I. A., Fawell, P. D., & Small, M. (2020). Particle-resolved direct numerical simulation of drag force on permeable, non-spherical aggregates. *Chemical Engineering Science*, 218, 115582.
- Monty, J. P., Stewart, J. A., Williams, R. C., & Chong, M. S. (2007). Large-scale features in turbulent pipe and channel flows. *Journal of Fluid Mechanics*, 589, 147–156.
- Morris, S. C., Stolpa, S. R., Slaboch, P. E., & Klewicki, J. C. (2007). Near-surface particle image velocimetry measurements in a transitionally rough-wall atmospheric boundary layer. *Journal of Fluid Mechanics*, 580, 319–338.
- Morrison, J. F., Mckeon, B. J., Jiang, W., & Smits, A. J. (2004). Scaling of the streamwise velocity component in turbulent pipe flow. *Journal of Fluid Mechanics*, 508, 99–131.
- Nadeem, M., Lee, J. H., Lee, J., & Sung, H. J. (2015). Turbulent boundary layers over sparsely-spaced rod-roughened walls. *International Journal of Heat and Fluid Flow*, 56, 16–27.
- Nagib, H. M., & Chauhan, K. A. (2008). Variations of von Kármán coefficient in canonical flows. *Physics of Fluids*, 20(10), 101518.
- Nagib, H. M., Chauhan, K. A., & Monkewitz, P. A. (2007). Approach to an asymptotic state for zero pressure gradient turbulent boundary layers. *Philosophical Transactions of the Royal Society of London A: Mathematical, Physical and Engineering Sciences*, 365(1852), 755–770.
- Nickels, T. B., Marusic, I., Hafez, S., Hutchins, N., & Chong, M. S. (2007). Some predictions of the attached eddy model for a high Reynolds number boundary layer. *Philosophical Transactions of the Royal Society of London A: Mathematical, Physical and Engineering Sciences*, 365(1852), 807–822.
- Österlund, J. M., Johansson, A. V., Nagib, H. M., & Hites, M. H. (2000). A note on the overlap region in turbulent boundary layers. *Physics of Fluids*, 12(1), 1–4.
- Pan, Y., & Banerjee, S. (1997). Numerical investigation of the effects of large particles on wall-turbulence. *Physics of Fluids*, 9, 3786.
- Pathikonda, G., & Christensen, K. T. (2017). Inner-outer interactions in a turbulent boundary layer overlying complex roughness. *Physical Review Fluids*, 2(4), 044603.
- Perry, A. E., & Chong, M. S. (1982). On the mechanism of wall turbulence. *Journal of Fluid Mechanics*, 119, 173–217.
- Perry, A. E., & Marusic, I. (1995). A wall-wake model for the turbulence structure of boundary layers. Part 1. Extension of the attached eddy hypothesis. *Journal of Fluid Mechanics*, 298, 361–388.
- Piomelli, U., & Balaras, E. (2002). Wall-layer models for large-eddy simulations. *Annual Review of Fluid Mechanics*, 34(1), 349–374.
- Rajagopalan, S., & Antonia, R. A. (1980). Interaction between large and small scale motions in a two-dimensional turbulent duct flow. *Physics of Fluids*, 23(6), 1101–1110.
- Renzo, M. D., & Urzay, J. (2018). Aerodynamic generation of electric fields in turbulence laden with charged inertial particles. *Nature Communications*, 9, 1676.

- Richter, D. H. (2015). Turbulence modification by inertial particles and its influence on the spectral energy budget in planar Couette flow. *Physics of Fluids*, *27*, 063304.
- Righetti, M., & Romano, G. P. (2004). Particle-fluid interactions in a plane near-wall turbulent flow. *Journal of Fluid Mechanics*, *505*, 93–121.
- Robinson, S. K. (1991). Coherent motions in the turbulent boundary layer. *Annual Review of Fluid Mechanics*, *23*(1), 601–639.
- Rudge, W. A. D. (1913). Atmospheric electrification during South African dust storms. *Nature*, *91*, 31–32.
- Salesky, S. T., & Anderson, W. (2018). Buoyancy effects on large-scale motions in convective atmospheric boundary layers: Implications for modulation of near-wall processes. *Journal of Fluid Mechanics*, *856*, 135–168.
- Sardina, G., Schlatter, P., Picano, F., Casciola, C. M., Brandt, L., & Henningson, D. S. (2012). Self-similar transport of inertial particles in a turbulent boundary layer. *Journal of Fluid Mechanics*, *706*, 584–596.
- Schmidt, D. S., Schmidt, R. A., & Dent, J. D. (1998). Electrostatic force on saltating sand. *Journal of Geophysical Research: Atmospheres*, *103*, 8997–9001.
- Schoppa, W., & Hussain, F. (2002). Coherent structure generation in near-wall turbulence. *Journal of Fluid Mechanics*, *453*, 57–108.
- Scrce, F. J. (1930). *Some characteristics of eddy motion in the atmosphere* (Meteorological Office Geophysical Memoirs, No. 52). London, England: His Majesty's Stationery Office.
- Serafimovich, A., Thomas, C., & Foken, T. (2011). Vertical & horizontal transport of energy & matter by coherent motions in a tall spruce canopy. *Boundary-Layer Meteorology*, *140*(3), 429–451.
- Sillero, J. A., Jimenez, J., & Moser, R. D. (2013). One-point statistics for turbulent wall-bounded flows at Reynolds numbers up to δ^+ approximate to 2000. *Physics of Fluids*, *25*, 105102.
- Sillero, J. A., Jimenez, J., & Moser, R. D. (2014). Two-point statistics for turbulent boundary layers & channels at Reynolds numbers up to δ^+ approximate to 2000. *Physics of Fluids*, *26*(10), 105109.
- Sippola, P., Kolehmainen, J., Ozel, A., Liu, X., Saarenrinne, P., & Sundaresan, S. (2018). Experimental and numerical study of wall layer development in a tribocharged fluidized bed. *Journal of Fluid Mechanics*, *849*, 860–884.
- Smits, A. J., McKeon, B. J., & Marusic, I. (2011). High-Reynolds number wall turbulence. *Annual Review of Fluid Mechanics*, *43*, 353–375.
- Squire, D. T., Baars, W. J., Hutchins, N., & Marusic, I. (2016). Inner-outer interactions in rough-wall turbulence. *Journal of Turbulence*, *17*(12), 1159–1178.
- Squire, D. T., Hutchins, N., Morrill-Winter, C., Schultz, M. P., Klewicki, J. C., & Marusic, I. (2017). Applicability of Taylor's hypothesis in rough & smooth-wall boundary layers. *Journal of Fluid Mechanics*, *812*, 398–417.
- Stow, C. D. (1969). Dust and sand storm electrification. *Weather*, *24*, 134–137.
- Talluru, K. M., Baidya, R., Hutchins, N., & Marusic, I. (2014). Amplitude modulation of all three velocity components in turbulent boundary layers. *Journal of Fluid Mechanics*, *746*, R1.
- Tay, G. F. K., Kuhn, D. C. S., & Tachie, M. F. (2015). Effects of sedimenting particles on the turbulence structure in a horizontal channel flow. *Physics of Fluids*, *27*, 025106.
- Tomkins, C. D. (1997). *A particle image velocimetry study of coherent structures in a turbulent boundary layer* (Master's Thesis). University of Illinois at Urbana-Champaign.
- Tomkins, C. D., & Adrian, R. J. (2003). Spanwise structure and scale growth in turbulent boundary layers. *Journal of Fluid Mechanics*, *490*, 37–74.
- Townsend, A. A. (1976). *The structure of turbulent shear flow* (2nd ed.). Cambridge, UK: Cambridge University Press.
- Tritton, D. J. (1967). Some new correlation measurements in a turbulent boundary layer. *Journal of Fluid Mechanics*, *28*(03), 439–462.
- Tsuji, Y., Marusic, I., & Johansson, A. V. (2016). Amplitude modulation of pressure in turbulent boundary layer. *International Journal of Heat and Fluid Flows*, *61*, 2–11.
- Tsuji, Y., & Morikawa, Y. (1982). LDV measurements of an air-solid two-phase flow in a horizontal pipe. *Journal of Fluid Mechanics*, *120*, 385–409.
- Tutkun, M., George, W. K., Delville, J., Stanislas, M., Johansson, P. B. V., Foucaut, J. M., & Coudert, S. (2009). Two-point correlations in high Reynolds number flat plate turbulent boundary layers. *Journal of Turbulence*, *10*(21), 1–23.
- Vallikivi, M., Ganapathisubramani, B., & Smits, A. J. (2015). Spectral scaling in boundary layers and pipes at very high Reynolds numbers. *Journal of Fluid Mechanics*, *771*, 303.
- Vallikivi, M., Hultmark, M., & Smits, A. J. (2015). Turbulent boundary layer statistics at very high Reynolds number. *Journal of Fluid Mechanics*, *779*, 371–389.
- Vincenti, P., Klewicki, J., Morrill-Winter, C., White, C. M., & Wosnik, M. (2013). Streamwise velocity statistics in turbulent boundary layers that spatially develop to high Reynolds number. *Experiments in Fluids*, *54*(12), 1629.
- Vreman, A. W. (2007). Turbulence characteristics of particle-laden pipe flow. *Journal of Fluid Mechanics*, *584*, 235–279.
- Waitukaitis, S. R., Lee, V., Pierson, J. M., Forman, S. L., & Jaeger, H. M. (2014). Size-dependent same-material tribocharging in insulating grains. *Physical Review Letters*, *112*(21), 218001.
- Wallace, J. M. (2016). Quadrant analysis in turbulence research: History and evolution. *Annual Review of Fluid Mechanics*, *48*, 131–158.
- Wang, G., Gu, H., & Zheng, X. (2020). Large scale structures of turbulent flows in the atmospheric surface layer with and without sand. *Physics of Fluids*, *32*, 106604.

- Wang, G., & Richter, D. H. (2019). Two mechanisms of modulation of very-large-scale motions by inertial particles in open channel flow. *Journal of Fluid Mechanics*, *868*, 538–559.
- Wang, G., Zheng, X., & Tao, J. (2017). Very large scale motions and PM10 concentration in a high-Re boundary layer. *Physics of Fluids*, *29*, 061701.
- Wang, G. H., & Zheng, X. J. (2016). Very large scale motions in the atmospheric surface layer: A field investigation. *Journal of Fluid Mechanics*, *802*, 464–489.
- Wang, J., Pan, C., & Wang, J. (2020). Characteristics of fluctuating wall-shear stress in a turbulent boundary layer at low-to-moderate Reynolds number. *Physical Review Fluids*, *5*, 074605.
- Wang, Z., Huang, B., Zhang, M., Wang, G., & Zhao, X. (2018). Experimental & numerical investigation of ventilated cavitating flow structures with special emphasis on vortex shedding dynamics. *International Journal of Multiphase Flow*, *98*, 79–95.
- Willert, C., Eisfelder, M., Stanislas, M., Klinner, J., & Talamelli, A. (2017). Near-wall statistics of a turbulent pipe flow at shear Reynolds numbers up to 40000. *Journal of Fluid Mechanics*, *862*, R5.
- Williams, E. R., Nathou, N., Hicks, E., Pontikis, C., & Bartholomew, M. J. (2009). The electrification of dust-lifting gust fronts (haboobs) in the Sahel. *Atmospheric Research*, *91*, 292–298.
- WMO (1983). *Guide to meteorological instruments & methods of observation* (5th ed.). Geneva, Switzerland: World Meteorological Organization.
- Yair, Y., Katz, S., Yaniv, R., Ziv, B., & Price, C. (2016). An electrified dust storm over the Negev desert, Israel. *Atmospheric Research*, *181*, 62–71.
- Yao, Y., Huang, W., & Xu, C. (2018). Amplitude modulation & extreme events in turbulent channel flow. *Acta Mechanica Sinica*, *34*(1), 1–9.
- Zeng, Q. C., Cheng, X., Hu, F., & Peng, Z. (2010). Gustiness & coherent structure of strong winds & their role in dust emission & entrainment. *Advances in Atmospheric Sciences*, *27*, 1–13.
- Zhang, H., Bo, T. L., & Zheng, X. (2017). Evaluation of the electrical properties of dust storms by multi-parameter observations and theoretical calculations. *Earth & Planetary Science Letters*, *461*, 141–150.
- Zhang, H., & Zheng, X. J. (2018). Quantifying the large-scale electrification equilibrium effects in dust storms using field observations at Qingtu lake observatory. *Atmospheric Chemistry and Physics*, *18*, 17087–17097.
- Zhang, H., & Zhou, Y. H. (2020a). Effects of 3D electric field on saltation during dust storms: an observational and numerical study. *Atmospheric Chemistry and Physics*, *20*(23), 14801–14820.
- Zhang, H., & Zhou, Y. H. (2020b). Reconstructing the electrical structure of dust storms from locally observed electric field data. *Nature Communications*, *11*, 5072.
- Zhang, Y. Y., Hu, R. F., & Zheng, X. J. (2018). Large-scale coherent structures of suspended dust concentration in the neutral atmospheric surface layer: A large-eddy simulation study. *Physics of Fluids*, *30*(4), 046601.
- Zhao, L., Andersson, H. I., & Gillissen, J. J. J. (2013). Interphasial energy transfer and particle dissipation in particle-laden wall turbulence. *Journal of Fluid Mechanics*, *715*(4), 32–59.
- Zheng, X. (2020). Reynolds number effects in turbulent boundary layer. *IUTAM Symposium*, under review.
- Zheng, X., Wang, G., & Zhu, W. (2021). Experimental study on the effects of particle-wall interactions on VLSM in sand-laden flows. *Journal of Fluid Mechanics*, *914*, A35.
- Zheng, X., Zhang, J., Wang, G., Liu, H., & Zhu, W. (2013). Investigation on very large scale motions (VLSMs) and their influence in a dust storm. *Science China Physics, Mechanics and Astronomy*, *56*(2), 306–314.
- Zheng, X. J. (2009). *Mechanics of wind-blown sand movements*. Berlin, Heidelberg, Germany: Springer.
- Zheng, X. J. (2013). Electrification of wind-blown sand: Recent advances and key issues. *European Physical Journal E Soft Matter*, *36*(12), 138.
- Zheng, X. J., Huang, N., & Zhou, Y. H. (2003). Laboratory measurement of electrification of wind-blown sands and simulation of its effect on sand saltation movement. *Journal of Geophysical Research Atmospheres*, *108*, 4322.
- Zhou, Y. H., He, Q. S., & Zheng, X. J. (2005). Attenuation of electromagnetic wave propagation in sandstorms incorporating charged sand particles. *The European Physical Journal E*, *17*(2), 181–187.